

THE X-RAY-TO-OPTICAL PROPERTIES OF OPTICALLY-SELECTED ACTIVE GALAXIES OVER WIDE LUMINOSITY AND REDSHIFT RANGES

A. T. STEFFEN¹, I. STRATEVA¹, W. N. BRANDT¹, D. M. ALEXANDER², A. M. KOEKEMOER³, B. D. LEHMER¹, D. P. SCHNEIDER¹,
C. VIGNALI^{4,5}

Submitted to the Astronomical Journal on October 12, 2005; Accepted February 17, 2006

ABSTRACT

We present partial-correlation analyses that examine the strengths of the relationships between $l_{2500 \text{ \AA}}$, $l_{2 \text{ keV}}$, α_{OX} , and redshift for optically-selected AGNs. We extend the work of Strateva et al. (2005), that analyzed optically-selected AGNs from the Sloan Digital Sky Survey (SDSS), by including 52 moderate-luminosity, optically-selected AGNs from the COMBO-17 survey with corresponding deep (≈ 250 ks to 1 Ms) X-ray observations from the Extended *Chandra* Deep Field-South. The COMBO-17 survey extends ~ 3 magnitudes deeper than the SDSS and probes the moderate-luminosity AGNs that numerically dominate the AGN population in the Universe. We also include recently published observations of 19 high-redshift, optically-selected AGNs, and 46 luminous, low-redshift AGNs from the Bright Quasar Survey. The full sample used in our analysis consists of 333 AGNs, extending out to $z \sim 6$, with 293 (88%) having X-ray detections. The sample spans five decades in UV luminosity and four decades in X-ray luminosity. We confirm that α_{OX} is strongly anti-correlated with $l_{2500 \text{ \AA}}$ (13.6σ), the highest significance found for this relation to date, and find evidence suggesting that the slope of this relation may be dependent on $l_{2500 \text{ \AA}}$. We find that no significant correlation exists between α_{OX} and redshift (1.3σ), and constrain the maximum evolution of AGN UV-to-X-ray flux ratios to be less than 30% (1σ) out to $z = 5$. Using our sample's high X-ray detection fraction, we also find a significant anti-correlation (3.0σ) between α_{OX} and $l_{2 \text{ keV}}$. We make comparisons to earlier studies on this topic and discuss implications for X-ray vs. optical luminosity functions.

Subject headings: Galaxies: Active: Nuclei — Galaxies: Active: Optical/UV/X-ray — Galaxies: Active: Evolution — Methods: Statistical

1. INTRODUCTION

The relationship between X-ray and UV luminosity for AGNs, defined by Tananbaum et al. (1979) as $\alpha_{\text{OX}} = \log[l(\nu_{\text{X-ray}})/l(\nu_{\text{UV}})]/\log(\nu_{\text{X-ray}}/\nu_{\text{UV}})$, where $l(\nu)$ is the monochromatic luminosity ($\text{erg s}^{-1} \text{ Hz}^{-1}$) at frequency ν in the rest-frame, has been the subject of many studies over the last two decades (e.g., Avni & Tananbaum 1982; Kriss & Canizares 1985; Avni & Tananbaum 1986; Anderson & Margon 1987; Wilkes et al. 1994; Vignali et al. 2003; Strateva et al. 2005). Most of these investigations examined the relationship between the 2500 \AA and 2 keV monochromatic luminosities, reducing the α_{OX} relationship to $\alpha_{\text{OX}} = 0.3838 \log(l_{2 \text{ keV}}/l_{2500 \text{ \AA}})$. These studies have usually found that α_{OX} is anti-correlated with UV luminosity, with at most a weak anti-correlation with redshift (but see Yuan et al. 1998; Bechtold et al. 2003). Understanding the relationship between the intrinsic UV and X-ray emission from AGNs and its evolution through cosmic time is important for testing energy generation models in AGNs, deriving bolometric corrections for AGNs which are used in estimating their luminosities and accretion rates, identifying X-ray weak AGNs, and estimating additional X-ray emission linked with jets in radio-loud AGNs. In addition, understanding how α_{OX} evolves with redshift aids in resolving discrepancies between the luminosity

functions derived from optical (e.g., Boyle et al. 2000; Wolf et al. 2003; Richards et al. 2005) and X-ray (e.g., Miyaji et al. 2000; Steffen et al. 2003; Ueda et al. 2003; Barger et al. 2005; Hasinger et al. 2005; La Franca et al. 2005) AGN samples, which map the evolution of the accretion onto supermassive black-holes (SMBHs) in the Universe.

To provide tight constraints upon $\alpha_{\text{OX}}(l, z)$, any degeneracies between luminosity and redshift must be broken. This is difficult in flux-limited samples, as l and z are typically strongly correlated. To obtain good coverage of the $l - z$ plane while maintaining a high X-ray detection fraction, it is necessary to combine both wide-field and deeper, narrow-field surveys. To achieve this goal we expand here upon the α_{OX} work of Strateva et al. (2005, hereafter S05), who used the wide-field Sloan Digital Sky Survey (SDSS; York et al. 2000) quasar sample along with low-redshift ($z < 0.2$) Seyfert 1s and high-redshift ($z > 4$) optically selected AGNs. We add to this sample moderate-luminosity, optically-selected AGNs from the deep, narrow-field (0.26 deg^2) COMBO-17 survey (Wolf et al. 2004) centered on the Extended *Chandra* Deep Field-South (E-CDF-S; Lehmer et al. 2005), along with a well-studied sample of luminous Bright Quasar Survey (BQS) quasars (Schmidt & Green 1983) at $z < 0.5$ and additional optically-selected AGNs at $z > 4$ (Kelly et al. 2005; Shemmer et al. 2005; Vignali et al. 2005). The AGNs optically selected in the COMBO-17 survey extend ~ 3 magnitudes fainter than those used in previous α_{OX} studies (e.g., $B = 19.2$; Avni & Tananbaum 1986 and $B = 19.5$; Anderson & Margon 1987) and have a substantially higher sky density than the SDSS quasar sample ($\sim 670 \text{ deg}^{-2}$ versus $\sim 10 \text{ deg}^{-2}$; Wolf et al. 2004; Schneider et al. 2005). These COMBO-17 AGNs are representative of most of the optically-selectable AGNs in the Universe.

¹ Department of Astronomy and Astrophysics, 525 Davey Laboratory, Pennsylvania State University, University Park, PA 16802.

² Institute of Astronomy, Madingley Road, Cambridge CB3 0HA, UK.

³ Space Telescope Science Institute, 3700 San Martin Drive, Baltimore, MD 21218.

⁴ Dipartimento di Astronomia, Università degli Studi di Bologna, Via Ranzani 1, 40127 Bologna, Italy.

⁵ INAF-Osservatorio Astronomico di Bologna, Via Ranzani 1, 40127 Bologna, Italy.

While deep X-ray surveys can provide even higher AGN sky densities (up to $\simeq 7000 \text{ deg}^{-2}$; e.g., Alexander et al. 2003), X-ray selected samples are dominated by obscured sources (e.g., Bauer et al. 2004). In the UV, this obscuration leads to increased contamination from the host galaxy and uncertain absorption corrections (e.g., Moran, Filippenko, & Chornock 2002). The X-ray absorption corrections are also often uncertain, mainly due to the poor signal-to-noise ratio of X-ray spectra with low photon counts. It is therefore difficult to measure the *intrinsic* emission from these obscured AGNs, and thus they do not significantly elucidate the intrinsic energy generation mechanisms within AGNs.

The exclusion of obscured sources from our analyses does not necessarily mean our conclusions below are valid for unobscured sources only. Our results are still applicable to obscured AGNs if the obscuration is a line-of-sight orientation effect and does not affect the intrinsic energy generation mechanisms within AGNs (i.e., if the ‘‘Unified’’ AGN model is valid; see Antonucci 1993, for a review). This will apply even given the recent evidence for luminosity-dependent obscuration found in X-ray selected AGN samples (e.g., Steffen et al. 2003; Ueda et al. 2003; Barger et al. 2005; La Franca et al. 2005).

We briefly introduce the optical and X-ray samples used in this paper in §2. In §3 we discuss the analysis of the correlations between $l_{2500 \text{ \AA}}$, $l_{2 \text{ keV}}$, α_{ox} , and redshift. We discuss our findings and present our conclusions in §4. We use J2000 coordinates and the cosmological parameters $H_0 = 70 \text{ km s}^{-1} \text{ Mpc}^{-1}$, $\Omega_M = 0.3$, and $\Omega_\Lambda = 0.7$.

2. SAMPLE

To search for correlations among $l_{2500 \text{ \AA}}$, $l_{2 \text{ keV}}$, α_{ox} , and redshift within optically-selected AGN samples, it is best to cover as much of the $l - z$ plane as possible to minimize degeneracies. It is also important to eliminate AGNs with intrinsic absorption that can affect UV and X-ray photons differently, and radio-loud AGNs that can have additional UV and X-ray flux associated with the radio jet (e.g., Worrall et al. 1987; Wilkes & Elvis 1987; Worrall & Birkinshaw 2005). To this end, we combine the data from S05 with the optically-selected, moderate-luminosity AGNs from the COMBO-17 survey, a subsample of sources from the BQS quasar catalog which includes higher-luminosity, optically-selected AGNs, and additional optically-selected, $z > 4$ AGNs. We describe our AGN sample below starting with a brief description of the S05 catalog.

2.1. Strateva et al. (2005) Sample

The main S05 sample is composed of broad-line AGNs optically selected via multi-band photometry in the SDSS Data Release 2 (SDSS DR2; Abazajian et al. 2004), excluding broad absorption-line quasars (BALQSOs) and radio-loud sources. The S05 sample is an unbiased subsample of the full SDSS DR2 AGN catalog, selecting sources with medium-deep ($> 11 \text{ ks}$) *ROSAT* PSPC observations. Of the 155 SDSS DR2 AGNs in the S05 sample, 126 (81%) have X-ray detections. X-ray upper limits were calculated for the remaining 29 sources. The 155 AGNs span redshifts $0.2 < z < 3.5$.

To extend their $l - z$ plane coverage, S05 include the low-redshift Seyfert 1 sample of Walter & Fink (1993), excluding the radio-loud sources ($L_{5 \text{ GHz}} > 10^{25} \text{ W Hz}^{-1}$). Twelve of these AGNs are also included in the well-defined BQS (see § 2.2.2), and thus we have removed them from the S05 sample. For their high-redshift sample, S05 include optically-

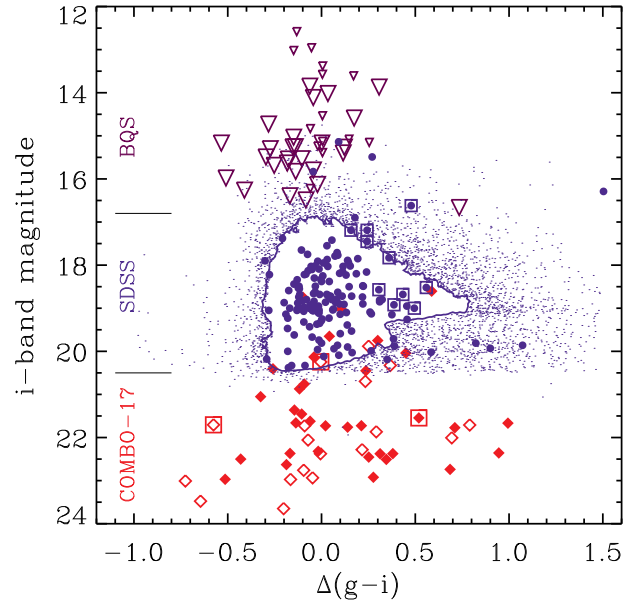


FIG. 1.— Apparent i -band PSF magnitude vs. relative $g - i$ color, $\Delta(g - i)$, for our selected COMBO-17 sample (red diamonds), the SDSS sample (blue circles), and the BQS sample (violet downward-pointing triangles). For comparison the full SDSS DR2 sample is shown as a blue contour enclosing 90% of the data and small blue dots representing the outliers. Any sources with significant galaxy contributions that could affect their observed colors (identified spectroscopically for SDSS AGNs and labeled ‘‘QSO (GAL?)’’ in the COMBO-17 survey) are enclosed by large squares. COMBO-17 sources with $z > 2.1$ are denoted by open diamonds. The BQS sample sources observed in the SDSS are denoted with large symbols, and sources with SDSS magnitudes derived from other bands are denoted with small symbols. In the computation of $\Delta(g - i)$, only AGNs with point-source morphology were used to determine the median $g - i$ color as a function of redshift to prevent artificial reddening due to host-galaxy contamination. The characteristic i -band magnitude ranges for the BQS, SDSS, and COMBO-17 samples are denoted along the left-hand side of the figure.

selected, $z > 4$ quasars from the SDSS, the Palomar Digital Sky Survey (Djorgovski et al. 1998), and the Automatic Plate Measuring facility survey (Irwin et al. 1991). These high-redshift AGNs were specifically targeted by *Chandra* and *XMM-Newton*, and S05 again eliminated radio-loud sources and BALQSOs from their sample. It is important to note that all of these optically-selected, high-redshift AGNs would have met the SDSS AGN color-selection criteria, so the introduction of the sources from other surveys does not bias the S05 sample. This high-redshift sample includes 36 AGNs, increasing the S05 total sample size to 216 optically-selected AGNs (after removing the twelve Seyfert 1s also observed in the BQS), 183 (85%) of which have detected X-ray counterparts and 33 (15%) of which have X-ray upper limits.

2.2. New Objects in This Study

2.2.1. COMBO-17

To extend the AGN sample to fainter luminosities we include the optically-selected AGNs from the portion of the COMBO-17 survey that covers the E-CDF-S (Wolf et al. 2004). To determine if the COMBO-17 AGNs are indeed consistent with being a fainter extension of the SDSS AGNs, we examine the color-magnitude distributions of the two populations. Figure 1 shows the apparent i -band PSF magnitudes versus the relative $g - i$ colors for the COMBO-17 AGNs (diamonds), the SDSS AGNs (circles), and the BQS sample

covered by SDSS (*large triangles*) and with SDSS colors derived from APM magnitudes (*small triangles*). The SDSS g and i magnitudes were calculated for the COMBO-17 AGNs using the observed $BVRi$ magnitudes and the color transformations calculated by Jester et al. (2005). These AGN color transformations are for sources with redshifts $z < 2.1$. In Figure 1 we denote COMBO-17 sources beyond this redshift with open diamonds. The relative $g-i$ colors, denoted as $\Delta(g-i)$, were constructed by subtracting the median $g-i$ color of the DR2 AGNs as a function of redshift from the observed $g-i$ color. Relative (i.e., redshift-corrected) colors can be used to detect significant differences in the optical/UV continua of AGNs (Richards et al. 2003), so they can be used to compare the SDSS and COMBO-17 AGN populations. From Figure 1 it appears that the COMBO-17 AGN sample is plausibly the faint extension of the SDSS AGN population.

The COMBO-17 survey used observations in 5 broad-band and 12 medium-band filters spanning the optical regime to derive photometric redshifts and “fuzzy” spectra for over 63 000 sources in the E-CDF-S field. Wolf et al. (2004) find 175 sources with photometric colors that are best matched by the SDSS broad-line QSO template spectrum of Vanden Berk et al. (2001). Their method preferentially selects broad-line AGNs, but narrow-line sources with strong AGN emission lines could also be selected.

The 17-band photometry and use of multiple galaxy/AGN templates allows the COMBO-17 survey to measure among the most accurate photometric redshifts to date. To examine the quality of the photometric redshifts for the COMBO-17 AGNs, we compared the photometric redshifts with a compilation of publicly available spectroscopic redshifts of sources within the GOODS-South field created by Alessandro Rettura.⁶ For our study, we find spectroscopic redshifts for 12 COMBO-17 AGNs and use photometric redshifts for the remaining sources. Overall, we find excellent agreement between the photometric and spectroscopic redshifts for AGNs at the magnitudes we consider below. The spectroscopic redshifts for 11 sources differ by less than 5% from their measured photometric redshifts. Only one of the twelve COMBO-17 sources with measured spectroscopic redshifts has a photometric redshift that significantly disagrees with the spectroscopic value (COMBO-17 ID: 30792; $z_{\text{phot}} = 1.929$; $z_{\text{spec}} = 0.743$).

To obtain monochromatic 2 keV X-ray luminosities (or upper limits) for these COMBO-17 AGNs, we match the sources to the E-CDF-S and the *Chandra* Deep Field-South (CDF-S; Alexander et al. 2003) X-ray catalogs. The E-CDF-S is composed of four 250 ks *Chandra* observations that cover the entire COMBO-17 field (Lehmer et al. 2005). The 1 Ms CDF-S probes fainter fluxes than the E-CDF-S, but it does not cover the entire COMBO-17 field. We use a $2''$ matching radius to identify the X-ray counterparts of the COMBO-17 AGNs, and we estimate the false-match probability to be $< 0.5\%$. All of the COMBO-17 sources with X-ray counterparts were detected in the E-CDF-S, and none had more than one X-ray counterpart. We use the CDF-S to derive X-ray upper limits only when COMBO-17 AGNs are not detected in the overlapping E-CDF-S fields.

To minimize potential contamination of our correlation analysis below we impose two unbiased selection criteria on the full COMBO-17 AGN sample. First, we only consider sources brighter than $R = 23$. At these magnitudes the probability of a COMBO-17 source being misidentified as an AGN is low ($\sim 1\%$; Wolf et al. 2004). In addition, at $R > 23$ the

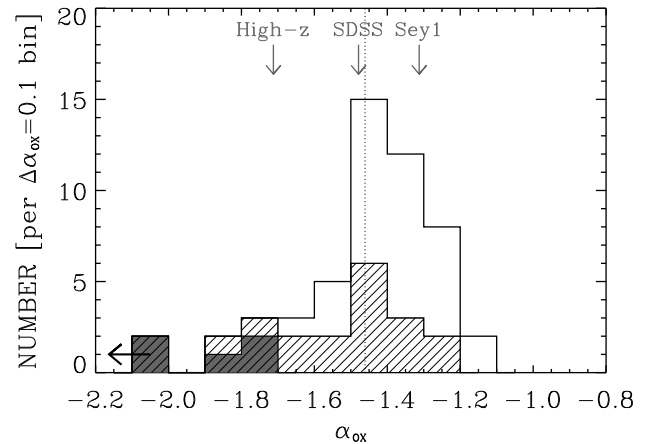


FIG. 2.— Histogram of the α_{OX} values for the 52 COMBO-17 AGNs included in our sample. The mean of the distribution is shown with a dotted line. COMBO-17 AGNs with $\Gamma < 1.6$ are marked (*hatched histogram*). Sources with α_{OX} upper-limits (i.e., without X-ray detections) are also marked (*shaded histogram*). The left-pointing arrow indicates the direction of the limits. For comparison, we show the mean α_{OX} values for the three AGN samples in S05, which are described in Table 3.

fraction of COMBO-17 AGNs with X-ray detections drops quickly. This magnitude threshold ensures that the fraction of AGNs with X-ray detections remains high, reducing the impact of X-ray limits in our analysis. Second, we only include sources that have *HST* ACS data from either the Galaxy Evolution from Morphology and SEDs survey (GEMS; Rix et al. 2004) or the Great Observatories Origins Deep Survey (GOODS; Giavalisco et al. 2004). These high-resolution data, which cover $\sim 84\%$ of the COMBO-17 field, can be used to minimize the galaxy contribution to the UV luminosity of the COMBO-17 sources identified as being extended objects (flagged as ‘QSO (GAL?)’ in Wolf et al. 2004). These two selection criteria reduce the COMBO-17 AGN sample from 175 to 60 sources, with 49 (82%) having X-ray detections and 13 (22%) identified as extended objects.

Using the high-resolution GEMS and GOODS ACS V-band images we identified four COMBO-17 AGNs (COMBO-17 IDs: 5498, 18324, 31898, and 50415) that were incorrectly classified as extended sources but are actually close sources blended together in the lower-resolution COMBO-17 images. We correct the COMBO-17 classification for these blended sources. For the remaining nine extended COMBO-17 AGNs, we attempted to minimize the contribution of the host galaxies to the measured optical/UV luminosities of the AGNs. Using the high-resolution ACS images we compared the magnitudes of the COMBO-17 AGNs using $3''$ and $0.5''$ apertures. A mean magnitude difference of 0.352 mag was calculated for the unresolved COMBO-17 AGNs. For the extended sources, we calculated the magnitude differences using the same aperture sizes. Any magnitude offsets exceeding the mean difference calculated for the point-like AGNs were considered to be caused by excess light from the host galaxy. We subtracted this host-galaxy contribution from the observed COMBO-17 R -band magnitude and found that six of the nine extended sources subsequently fell below our $R = 23$ magnitude limit. Since these extended AGNs would not have met our magnitude criterion without the ad-

⁶ Available at http://www.eso.org/science/goods/spectroscopy/CDFS_Mastercat/

TABLE 1
 COMBO-17/E-CDF-S AGN DATA.

COMBO-17 ID (1)	E-CDF-S ID (2)	α_{J2000} (3)	δ_{J2000} (4)	z (5)	$\log(f_{2500 \text{ \AA}})$ [erg cm ⁻² s ⁻¹ Hz ⁻¹] (6)	$\log(l_{2500 \text{ \AA}})$ [erg s ⁻¹ Hz ⁻¹] (7)	$\log(f_2 \text{ keV})$ [erg cm ⁻² s ⁻¹ Hz ⁻¹] (8)	$\log(l_2 \text{ keV})$ [erg s ⁻¹ Hz ⁻¹] (9)	α_{OX} (10)	Γ (11)	R (12)
1257	399	03 32 32.28	-28 03 28.2	1.231	-28.19	29.40	-31.51	26.08	-1.27	1.49	< 3.20
1731	678	03 33 22.85	-28 03 12.9	1.499	-28.47	29.29	-32.20	25.56	-1.43	2.04	< 5.79
2006	397	03 32 32.00	-28 03 09.9	1.966	-27.37	30.60	-31.12	26.85	-1.44	1.56	< 0.43
4050	357	03 32 20.31	-28 02 14.7	1.635	-27.80	30.03	-31.53	26.29	-1.43	1.89	< 1.17
4809	99	03 31 36.25	-28 01 49.6	1.988	-28.31	29.67	-31.72	26.26	-1.31	1.79	< 3.51
4995	234	03 31 56.88	-28 01 49.1	1.412	-28.50	29.21	-32.39	25.31	-1.49	1.87	< 5.65
5498 ^a	630	03 33 16.07	-28 01 31.3	2.075	-28.45	29.56	-31.97	26.04	-1.35	1.62	< 7.22
6735	566	03 33 06.26	-28 00 55.5	2.444	-28.32	29.82	-31.99	26.14	-1.41	1.89	< 3.91
6817	53	03 31 27.79	-28 00 51.0	1.988	-28.04	29.94	-31.96	26.02	-1.51	1.49	< 2.33
7570 ^b	...	03 33 08.03	-28 00 30.8	3.583	-27.44	30.97	< -32.81	< 25.60	< -2.06	...	< 4.18
7671	198	03 31 51.80	-28 00 25.7	2.436	-28.44	29.69	-31.97	26.17	-1.35	1.94	< 4.47
11818	...	03 32 55.98	-27 58 45.3	4.021	-28.26	30.23	< -33.47	< 25.53	< -1.80	...	< 36.14
11922	587	03 33 09.11	-27 58 26.6	2.539	-28.33	29.84	-32.02	26.45	-1.30	1.42	< 6.67
11941	699	03 33 26.24	-27 58 29.7	2.172	-27.74	30.30	-31.39	26.46	-1.48	2.12	< 1.07
12325	541	03 33 01.70	-27 58 18.8	1.843	-27.64	30.28	-31.17	26.66	-1.39	1.51	< 0.66
13332	600	03 33 10.63	-27 57 48.5	1.602	-27.99	29.82	-31.53	26.19	-1.39	1.97	< 2.11
15396	343	03 32 16.13	-27 56 44.1	2.682	-28.39	29.81	-32.68	25.64	-1.60	1.33	< 6.72
15731	711	03 33 28.93	-27 56 41.1	0.835	-27.65	29.61	-30.82	26.29	-1.28	1.82	< 0.78
16621	595	03 33 09.70	-27 56 13.9	2.540	-27.47	30.69	-32.05	26.44	-1.63	1.80	< 0.60
17229	...	03 32 22.57	-27 55 54.4	2.870	-28.54	29.71	< -33.20	< 25.07	< -1.78	...	< 14.68
18256	677	03 33 22.79	-27 55 23.7	1.647	-27.78	30.05	-31.93	26.06	-1.53	2.01	< 1.14
18324 ^a	531	03 33 00.77	-27 55 20.6	1.990	-28.43	29.55	-31.43	26.47	-1.18	2.23	< 6.82
19965	154	03 31 45.20	-27 54 35.6	0.634	-27.51	29.51	-31.22	25.47	-1.55	1.92	< 0.55
25042	434	03 32 41.85	-27 52 02.4	3.610 ^c	-28.08	30.34	-32.02	26.48	-1.48	1.43	< 12.09
25884	95	03 31 35.77	-27 51 34.7	1.630	-28.14	29.68	-31.43	26.39	-1.26	1.67	< 3.61
30792	440	03 32 43.24	-27 49 14.1	0.743 ^c	-28.60	28.56	-31.79	25.14	-1.31	1.66	< 5.72
33069	308	03 32 09.45	-27 48 06.7	2.810 ^c	-27.53	30.71	-32.23	26.04	-1.79	0.82	< 1.41
33630	119	03 31 40.12	-27 47 46.4	2.719	-28.32	29.90	-31.99	26.23	-1.41	1.59	< 3.72
33644	525	03 32 59.85	-27 47 48.2	2.538	-28.15	30.02	-31.74	26.76	-1.25	1.71	< 2.35
34357	304	03 32 08.67	-27 47 34.2	0.543 ^c	-27.33	29.55	-30.55	25.89	-1.40	1.73	13.89
36120	180	03 31 49.41	-27 46 34.0	2.306	-28.35	29.74	-32.09	25.85	-1.49	1.42	< 5.10
37487	422	03 32 39.08	-27 46 01.8	1.216 ^c	-27.86	29.73	-32.68	25.01	-1.81	1.07	< 1.25
38551	390	03 32 29.98	-27 45 29.8	1.221 ^c	-28.03	29.56	-31.53	26.00	-1.37	1.66	< 1.88
38905	549	03 33 03.62	-27 45 18.7	1.264	-28.71	28.90	-32.05	25.66	-1.25	1.55	< 11.94
39432	393	03 32 30.22	-27 45 04.5	0.735 ^c	-28.52	28.63	-31.85	25.33	-1.27	1.88	< 4.83
42601 ^b	515	03 32 59.07	-27 43 39.5	0.510	-27.98	28.85	-31.52	24.90	-1.51	1.67	< 3.60
43151	249	03 32 00.36	-27 43 19.5	1.037 ^c	-28.42	29.03	-31.70	25.48	-1.36	1.54	< 4.70
44126	583	03 33 08.78	-27 42 54.4	0.729	-28.91	28.23	-31.78	25.06	-1.22	1.74	< 11.20
47615	191	03 31 50.96	-27 41 15.7	0.649	-28.52	28.52	-31.96	25.11	-1.31	1.79	< 5.92
48284	378	03 32 27.01	-27 41 04.9	0.734 ^c	-27.16	29.99	-30.61	26.25	-1.43	1.79	5.59
48870	712	03 33 28.94	-27 40 43.7	2.146	-28.46	29.57	-31.68	26.66	-1.12	1.61	< 5.64
49298	374	03 32 26.49	-27 40 35.5	1.031 ^c	-27.52	29.93	-31.37	26.03	-1.49	2.08	< 0.61
50415 ^a	412	03 32 37.45	-27 40 00.1	0.666 ^c	-28.89	28.17	-32.21	24.73	-1.32	1.83	< 11.25
50997	416	03 32 38.12	-27 39 44.8	0.837 ^c	-27.71	29.55	-31.38	25.90	-1.40	2.05	< 0.92
51835	118	03 31 40.05	-27 39 17.6	2.179	-28.60	29.45	-32.51	25.63	-1.47	1.50	< 7.73
52963	...	03 32 52.60	-27 38 46.2	0.548	-28.67	28.22	< -33.30	< 23.59	< -1.78	...	< 7.38
54839	116	03 31 39.25	-27 37 52.0	1.428	-28.34	29.38	-31.88	26.04	-1.28	1.88	< 4.61
54969 ^b	...	03 32 49.28	-27 37 56.7	3.361	-27.39	30.97	< -33.09	< 25.61	< -2.06	...	< 1.23
56074	320	03 32 11.65	-27 37 25.9	1.574	-26.96	30.83	-31.13	26.84	-1.53	1.44	19.50
57653	35	03 31 23.53	-27 36 31.6	1.653	-28.25	29.58	-32.70	25.25	-1.66	1.40	< 3.74
58478	516	03 32 59.19	-27 36 11.7	1.348	-28.01	29.66	-32.05	25.77	-1.49	2.12	< 2.55
60939	245	03 31 58.91	-27 35 16.1	2.794	-28.29	29.94	-32.37	26.21	-1.43	0.96	< 7.46

^aSource is blended with nearby sources in COMBO-17 images.

^bSource is identified as 'QSO (GAL?)' in the COMBO-17 survey.

^cSpectroscopic redshift

ditional flux from the host galaxy, we exclude them from our sample, reducing it to 54 sources. None of these six AGNs has an X-ray detection.

We attempted to remove both radio-loud and obscured AGNs from our sample of COMBO-17 AGNs. Using 1.4 GHz VLA radio maps covering the COMBO-17 field (Kellermann et al. 2004) we found that only five of the 54 COMBO-17 AGNs have detected radio counterparts. We used the 1.4 GHz flux limit of $40 \mu\text{Jy}$ (5σ), quoted by Kellermann et al. (2004), as an upper limit for the undetected radio sources. We calculated the radio-loudness parameter, R , using the COMBO-17 B -band monochromatic flux ($\lambda = 4350 \text{ \AA}$) and converting the observed 1.4 GHz flux density to rest-frame 5 GHz, assuming $S(\nu) \propto \nu^{-0.8}$. We eliminate the

two COMBO-17 AGNs with $R > 30$, and give the values (or limits) of R for the remaining sources in Table 1. Our final COMBO-17 AGN sample consists of 52 sources, with 47 (90%) having X-ray counterparts.

We interpolate the optical data to find the monochromatic luminosity at 2500 \AA for each COMBO-17 source using the redshifts and the 12 medium-band photon fluxes given by Wolf et al. (2004). These bands range between $4180 - 9140 \text{ \AA}$ which, for rest-frame 2500 \AA , corresponds to a redshift range of $0.67 < z < 2.66$. For the 15 sources outside of this redshift range we linearly extrapolate to find the 2500 \AA luminosity. We calculated the monochromatic 2 keV luminosities from the $0.5 - 2 \text{ keV}$ luminosities, assuming a power-law spectral energy distribution (SED) with $\Gamma = 2.0$. Table 1

TABLE 2
BQS/ROSATAGN DATA.

Name	α_{J2000}	δ_{J2000}	z	$\log(f_{2500\text{\AA}})$ [erg cm ⁻² s ⁻¹ Hz ⁻¹]	$\log(l_{2500\text{\AA}})$ [erg s ⁻¹ Hz ⁻¹]	$\log(f_{2\text{ keV}})$ [erg cm ⁻² s ⁻¹ Hz ⁻¹]	$\log(l_{2\text{ keV}})$ [erg s ⁻¹ Hz ⁻¹]	α_{OX}
(1)	(2)	(3)	(4)	(5)	(6)	(7)	(8)	(9)
PG 0026+129	00 29 13.8	+13 16 05	0.142	-25.47	30.20	-29.21	26.46	-1.44
PG 0050+124	00 53 34.9	+12 41 36	0.061	-25.24	29.69	-28.96	25.96	-1.43
PG 0052+251	00 54 52.2	+25 25 39	0.155	-25.51	30.24	-29.12	26.64	-1.39
PG 0157+001	01 59 50.25	+00 23 40.8	0.164	-25.73	30.07	-29.83	25.97	-1.57
PG 0804+761	08 10 58.5	+76 02 43	0.100	-25.01	30.35	-28.91	26.45	-1.50
PG 0838+770	08 44 45.3	+76 53 10	0.131	-25.79	29.81	-29.76	25.84	-1.52
PG 0844+349	08 47 42.47	+34 45 04.4	0.064	-25.40	29.57	-30.28	24.69	-1.87
PG 0923+201	09 25 54.7	+19 54 04	0.190	-25.64	30.29	-29.59	26.34	-1.52
PG 0947+396	09 50 48.39	+39 26 50.5	0.206	-26.05	29.96	-29.60	26.41	-1.36
PG 0953+414	09 56 52.39	+41 15 22.2	0.239	-25.50	30.64	-29.50	26.64	-1.54
PG 1012+008	10 14 54.90	+00 33 37.4	0.185	-25.83	30.08	-30.02	25.89	-1.61
PG 1048+342	10 51 43.8	+33 59 26	0.167	-25.94	29.88	-29.85	25.97	-1.50
PG 1049-005	10 51 51.50	-00 51 17.7	0.357	-25.76	30.74	-30.18	26.32	-1.70
PG 1114+445	11 17 06.40	+44 13 33.3	0.144	-25.88	29.81	-30.14	25.54	-1.64
PG 1115+407	11 18 30.29	+40 25 54.0	0.154	-26.06	29.69	-29.86	25.89	-1.46
PG 1116+215	11 19 08.8	+21 19 18	0.177	-25.26	30.62	-29.35	26.52	-1.57
PG 1121+422	11 24 39.18	+42 01 45.0	0.234	-26.15	29.97	-29.88	26.24	-1.43
PG 1151+117	11 53 49.27	+11 28 30.4	0.176	-25.90	29.96	-29.56	26.30	-1.40
PG 1202+281	12 04 42.1	+27 54 12	0.165	-26.07	29.73	-29.52	26.29	-1.32
PG 1211+143	12 14 17.7	+14 03 13	0.085	-25.04	30.18	-28.85	26.37	-1.46
PG 1216+069	12 19 20.93	+06 38 38.5	0.334	-25.72	30.72	-29.58	26.86	-1.48
PG 1229+204	12 32 03.6	+20 09 30	0.064	-25.48	29.49	-29.15	25.82	-1.41
PG 1259+593	13 01 12.93	+59 02 06.8	0.472	-25.69	31.06	< -30.20	< 26.55	< -1.73
PG 1307+085	13 09 47.00	+08 19 48.2	0.155	-25.54	30.21	-29.47	26.29	-1.51
PG 1322+659	13 23 49.52	+65 41 48.2	0.168	-25.83	29.99	-29.56	26.26	-1.43
PG 1352+183	13 54 35.6	+18 05 18	0.158	-25.78	29.99	-29.59	26.18	-1.46
PG 1354+213	13 56 32.8	+21 03 51	0.300	-26.29	30.06	-29.98	26.37	-1.42
PG 1402+261	14 05 16.2	+25 55 34	0.164	-25.62	30.19	-29.45	26.35	-1.47
PG 1404+226	14 06 21.9	+22 23 47	0.098	-26.10	29.25	-29.51	25.83	-1.31
PG 1415+451	14 17 00.82	+44 56 06.4	0.114	-25.95	29.52	-29.97	25.51	-1.54
PG 1416-129	14 19 03.8	-13 10 45	0.129	-25.12	30.47	-29.17	26.42	-1.55
PG 1426+015	14 29 06.57	+01 17 06.1	0.086	-25.13	30.10	-28.91	26.32	-1.45
PG 1427+480	14 29 43.07	+47 47 26.2	0.221	-26.09	29.98	-29.96	26.11	-1.49
PG 1435-067	14 38 16.2	-06 58 20	0.129	-25.39	30.20	-29.47	26.12	-1.56
PG 1440+356	14 42 07.47	+35 26 23.0	0.077	-25.52	29.61	-29.03	26.10	-1.35
PG 1444+407	14 46 45.94	+40 35 05.8	0.267	-25.85	30.39	-29.98	26.26	-1.59
PG 1519+226	15 21 14.3	+22 27 44	0.137	-25.86	29.78	-29.95	25.69	-1.57
PG 1543+489	15 45 30.24	+48 46 09.1	0.400	-26.00	30.61	-30.47	26.14	-1.72
PG 1552+085	15 54 44.58	+08 22 21.5	0.119	-25.81	29.71	-30.13	25.38	-1.66
PG 1612+261	16 14 13.20	+26 04 16.2	0.131	-25.77	29.83	-29.15	26.45	-1.30
PG 1613+658	16 13 57.2	+65 43 10	0.129	-25.78	29.81	-29.09	26.50	-1.27
PG 1617+175	16 20 11.2	+17 24 28	0.114	-25.32	30.16	-29.67	25.81	-1.67
PG 1626+554	16 27 56.2	+55 22 32	0.133	-25.87	29.74	-29.34	26.27	-1.33
PG 2130+099	21 32 27.82	+10 08 19.2	0.061	-25.20	29.72	-28.96	25.97	-1.44
PG 2214+139	22 17 12.26	+14 14 20.9	0.067	-25.44	29.57	-30.66	24.35	-2.00
PG 2233+134	22 36 07.68	+13 43 55.3	0.325	-25.90	30.52	-30.03	26.39	-1.59

lists the properties of the COMBO-17 AGN sample, including the COMBO-17 ID from Wolf et al. (2004), the E-CDF-S ID from Lehmer et al. (2005), the sources' positions and redshifts, monochromatic 2500 Å and 2 keV fluxes and luminosities, α_{OX} , the effective X-ray power-law photon index (Γ), R , and a column identifying blended or extended COMBO-17 AGNs.

Since the majority of the COMBO-17 AGNs do not have optical spectra, we cannot easily identify obscured AGNs (using emission-line and absorption-line diagnostics) that may contaminate our sample. To identify potential obscured COMBO-17 AGNs, we will test the α_{OX} correlations below after removing the 22 sources with an effective X-ray power-law photon index $\Gamma < 1.6$, which is indicative of X-ray obscuration (Lehmer et al. 2005). This procedure does not help to identify potential obscured AGNs in the small number of COMBO-17 sources without X-ray counterparts; these sources will need future spectroscopic observations to identify possible absorption.

The α_{OX} distribution of our COMBO-17 AGN sample is

shown in Figure 2. COMBO-17 AGNs that have measured effective photon indices of $\Gamma < 1.6$, and sources that have α_{OX} upper-limits, are shown as hatched and shaded histograms, respectively. The COMBO-17 AGNs typically have flatter α_{OX} values than those calculated for more luminous AGN samples. This is consistent with the observed anti-correlation between α_{OX} and optical/UV luminosity seen in the studies mentioned in Section 1, where the value of α_{OX} falls with increasing $l_{2500\text{\AA}}$. For comparison, we mark the mean α_{OX} values for the three AGN samples used in S05 in Figure 2.

2.2.2. Bright Quasar Survey

To increase the luminosity range covered at low redshifts we included a set of 46 BQS quasars with $z < 0.5$ analyzed by Brandt, Laor, & Wills (2000). While the BQS sample does extend beyond $z = 0.5$, Jester et al. (2005) found a bias against detecting AGNs in the BQS catalog in the redshift range $0.5 < z < 1.0$. Since the BQS sample is meant to be a higher-luminosity complement to the S05 and Seyfert 1 samples at low redshifts, we removed 21 AGNs with $M_B > -23$.

This luminosity threshold also removes fainter AGNs that are more likely to be affected by contamination from their host galaxies. We excluded 13 radio-loud AGNs and five known BALQSOs (see footnote 4 in Brandt et al. 2000). In addition, following the arguments of Brandt et al. (2000), we also exclude two BQS quasars that have significant UV absorption, but do not meet the formal criteria for BALQSOs: PG 1351 + 640 (e.g., Zheng et al. 2001) and PG 1411 + 442 (e.g., Malkan et al. 1987).

We converted the $f_{3000\text{Å}}$ values used in Brandt et al. (2000) to $l_{2500\text{Å}}$, assuming $f(\nu) \propto \nu^{-\alpha}$ with $\alpha = -0.5$. We used PIMMS⁷ to calculate the monochromatic 2 keV luminosity, assuming a power-law spectrum with $\Gamma = 2$, from the *ROSAT* 0.5 – 2.0 keV pointed PSPC count-rate when available, and from the 0.5 – 2.0 keV *ROSAT* All Sky Survey (RASS) count-rate when no pointed *ROSAT* observation existed. An X-ray upper limit for one BQS quasar with no X-ray counterpart was calculated from the RASS. Our BQS sample contains 46 sources, with 45 (98%) having X-ray detections. We use the astrometry presented in Jester et al. (2005) for the BQS sources included therein and the astrometry from Véron-Cetty & Véron (2003) for the remaining sources. Table 2 presents the BQS sources’ names, positions, and redshifts along with the monochromatic 2500 Å and 2 keV fluxes and luminosities, and α_{ox} .

2.2.3. Additional High- z AGNs

To increase the size of our high-redshift sample we included recently published, optically-selected AGNs with $z > 4$. We included the ten luminous quasars listed in Table 3 of Vignali et al. (2005) (excluding the BALQSO PSS 1506 + 5220), and three radio-quiet AGNs from Shemmer et al. (2005) that were not included in S05 (Q 0000 – 263, BR 0351 – 1034, and BR 2237 – 0607). To extend the coverage of our sample to somewhat lower luminosities at $z > 4$ we included a sample of six optically-selected, faint, radio-quiet, non-BALQSO sources targeted in > 10 ks *Chandra* observations (Kelly et al. 2005). We analyzed these X-ray and optical data in the same manner as outlined in Vignali et al. (2005). We briefly present these data in the Appendix. The addition of these three optically-selected, $z > 4$ AGN samples adds 19 optically-selected AGNs to our total sample, 18 (94%) of which have X-ray detections.

For comparison purposes, we also plot the eight⁸ published X-ray-selected, radio-quiet, $z > 4$, AGNs (crosses) in Figures 3–9. We present the observed properties of these sources in Table A2 in the Appendix. While these X-ray-selected AGNs substantially extend the coverage of the UV luminosity - redshift plane at high redshifts (see Figure 3a), we do not include these AGNs in our formal analyses as they have been selected with different criteria than the other optically-selected AGN samples. However, in §4.3 we discuss how these AGNs fit into the relations derived in §3 using the optically-selected AGN samples.

⁷ Portable Interactive Multi-Mission Simulator available at <http://heasarc.gsfc.nasa.gov/Tools/w3pimms.html>

⁸ We excluded the two known X-ray-selected, radio-loud, $z > 4$ AGNs, RX J1028.6-0844 ($z = 4.28$; Zickgraf et al. 1997) and RX J1759.4+6638 ($z = 4.32$; Henry et al. 1994). An up-to-date compilation of $z > 4$ AGNs with X-ray detections is available at <http://www.astro.psu.edu/users/niel/papers/highz-xray-detected.dat>

TABLE 3
SUMMARY OF SAMPLES UTILIZED

Sample	Total AGNs	Number X-ray Detected	0.5 – 2.0 keV Limit [erg cm ⁻² s ⁻¹]	Area [sq. deg.]
S05				
SDSS	155	126 (81%)	$\sim 10^{-14}$	15
Seyfert 1	25 ^a	25 (100%)	$\sim 10^{-12}$... ^b
High- z	36	32 (89%)	$\sim 10^{-15}$... ^b
This work				
COMBO-17	52	47 (90%)	$\sim 10^{-16}$	0.26
BQS	46	45 (98%)	$\sim 10^{-13}$	10, 714
High- z	19	18 (95%)	$\sim 10^{-15}$... ^b
Full Sample				
Total	333	293 (88%) ^b

^aAfter removing the twelve sources that overlap with the BQS sample.

^bNot well defined.

2.3. Full Sample

The full sample used in our analysis consists of 333 AGNs, 293 (88%) of which have X-ray detections; this is a much higher X-ray detection fraction than for most previous analyses, where the detection fraction is typically 10 – 50%. The number of AGNs contributed by each sample, and their respective X-ray detection fractions, are summarized in Table 3. Figure 3 shows the monochromatic 2500 Å (*left*) and 2 keV (*right*) luminosity versus redshift for the combined AGN sample. The addition of the COMBO-17 (*diamonds*) and BQS (*downward-pointing triangles*) AGNs to the S05 data substantially improves the luminosity range covered out to $z \sim 3$, corresponding to $\simeq 85\%$ of cosmic history.

3. PARTIAL CORRELATION AND LINEAR REGRESSION ANALYSES

To measure properly the correlations among $l_{2500\text{Å}}$, $l_{2\text{keV}}$, α_{ox} , and redshift, we must attempt to eliminate (or minimize) potential sources of bias from our analysis. Following the arguments of Kembhavi, Feigelson, & Singh (1986), we use the AGN luminosities in our calculations and not the measured fluxes which, if used, can yield different results depending upon the cosmology and k -corrections assumed. However, using the luminosities can introduce a different bias since luminosity and redshift are typically correlated in flux-limited samples. Our sample was constructed to cover a large area of the $l - z$ plane, which acts to break this degeneracy.

While the majority of the AGNs in our sample have X-ray detections (88%), we cannot overlook the effects of sources with X-ray upper limits. In addition, our sample data undoubtedly contain intrinsic scatter that is not quantified in our measurements. We have minimized the effects of some sources of intrinsic scatter such as host-galaxy contamination, obscuration, and excess UV and X-ray flux associated with radio jets (as discussed in §2.2.1). Another source of intrinsic scatter in our data is caused by AGN variability, which affects our calculations of α_{ox} since the optical and X-ray observations were not taken concurrently. Unfortunately, the effects of variability cannot be corrected and remain a significant source of intrinsic scatter in our data. To measure the aforementioned correlations among these AGNs, proper statistical tools must be used that take these issues into consideration.

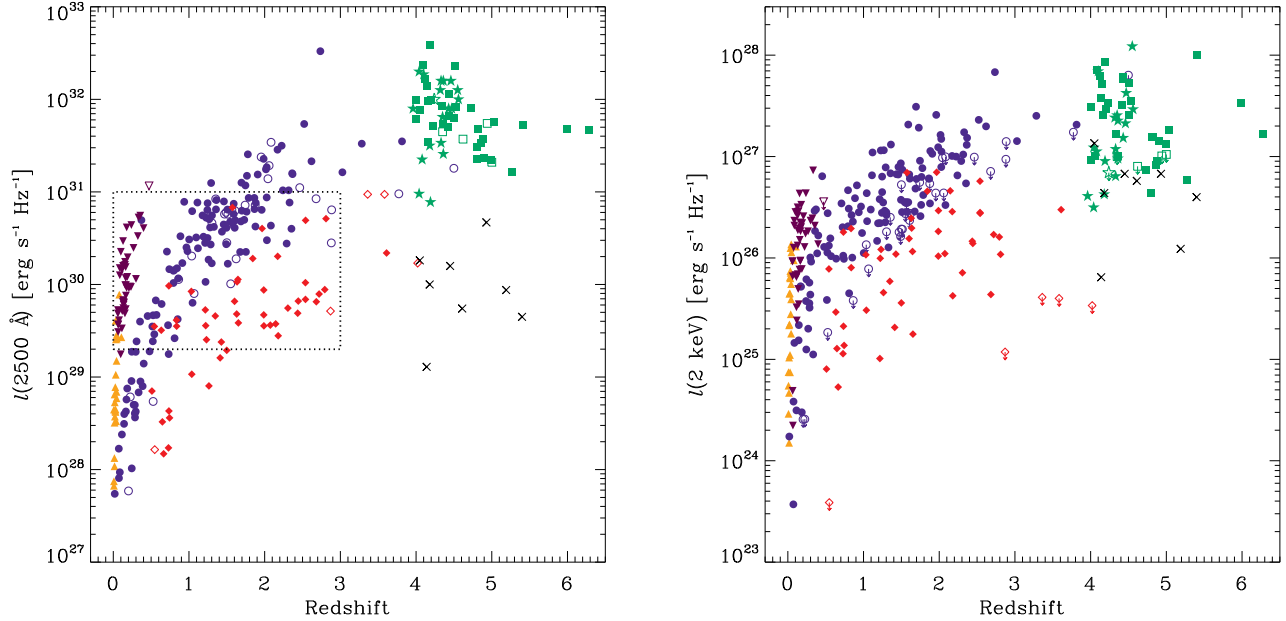


FIG. 3.— 2500 Å luminosity (*left*) and 2 keV luminosity (*right*) vs. redshift for the S05 Seyfert 1 (orange upward-pointing triangles), SDSS (blue circles), and high-redshift (green boxes) samples shown with the COMBO-17 (red diamonds), BQS (violet downward-pointing triangles), and optically selected, high-redshift AGNs (green stars). X-ray upper limits are represented using open symbols (*left*) or arrows (*right*). The $l_{2500 \text{ \AA}}$ - z subsample of 187 sources used in §3.6 is denoted by the dotted-line box (*left*). The properties of the known X-ray-selected AGNs at $z > 4$ (black crosses) are also shown; these sources are not included in our formal analyses due to their different selection criteria.

3.1. Statistical Tools

While our extended coverage of the $l - z$ plane helps to break the redshift bias introduced by using luminosities instead of fluxes in our analysis, a correlation between l and z can still be clearly seen in Figure 3. To take into account this existing correlation we use a partial-correlation analysis method that is designed to measure the correlation between two variables, controlling for the effects of one or more additional variables. A partial-correlation method that properly handles censored data was developed by Akritas & Siebert (1996). This method builds upon Kendall’s rank-correlation coefficient (Kendall 1938) and Kendall’s partial rank-correlation coefficient (Kendall 1970) to include censored data. To measure the partial correlations we use the FORTRAN program CENS_TAU, available from the Penn State Center for Astrostatistics⁹, which uses the methodology presented in Akritas & Siebert (1996). We present the results of our partial-correlation analysis in Table 4. In this table we also present the significance of the correlations with the potentially obscured ($\Gamma < 1.6$, see § 2.2.1) COMBO-17 AGNs removed. With the exception of a slight decrease in the significance in the $l_{2 \text{ keV}} - l_{2500 \text{ \AA}}$ correlation, there is no substantial change in the results when these sources are removed. Therefore, we use the full sample in our subsequent analyses.

To derive the linear-regression parameters for correlations, we use the Astronomy SURVival Analysis software package (ASURV Rev 1.2; Isobe et al. 1990; Lavalley et al. 1992), which implements the bivariate data-analysis methods presented in Isobe, Feigelson, & Nelson (1986). ASURV also properly handles censored data using the survival-analysis methods presented in Feigelson & Nelson (1985) and Isobe et al. (1986). We performed linear regressions using both

the fully parametric EM (estimate and maximize) regression algorithm (Dempster, Laird, & Rubin 1977) and the semi-parametric Buckley-James regression algorithm (Buckley & James 1979). The EM Regression algorithm uses an iterative least squares (ILS) method that reduces to the traditional ordinary least squares (OLS) when no censored data are present. We present the parameters provided by the EM regression algorithm below, but in all cases the results from the Buckley-James regression algorithm agreed within the errors.

3.2. $l_{2 \text{ keV}}$ versus $l_{2500 \text{ \AA}}$

Early X-ray studies of AGNs revealed a correlation between X-ray and UV monochromatic luminosities, typically found to be $l_X \propto l_{UV}^\beta$, where $\beta \simeq 0.7 - 0.8$ (see the references in §1). The observational evidence that β is not unity was unexpected and led to suggestions that this finding was not an intrinsic property of AGNs, but rather an observational bias introduced as a result of the larger scatter of l_{UV} compared to l_X (e.g., Chanan 1983; Yuan et al. 1998). La Franca et al. (1995) found an $l_X - l_{UV}$ correlation consistent with $\beta = 1$ using a generalized orthogonal regression procedure that takes into account measurement errors on both variables and intrinsic scatter. However, this method does not properly take into account the effects of censored data, which typically affect optically-selected AGN samples. Currently there is no statistical analysis method that properly handles data with both censoring and measurement errors (M. Akritas 2005, private communication).

For our optically-selected AGN sample we find a highly significant (15.3σ) correlation between the observed monochromatic X-ray and UV luminosities. The EM linear-regression algorithm in ASURV that we use to calculate the linear-regression parameters is based on the traditional ordinary least-squares method, $OLS(Y | X)$, which minimizes the residuals of the dependent variable, Y (the EM method

⁹ Available at http://www.astrostatistics.psu.edu/statcodes/cens_tau

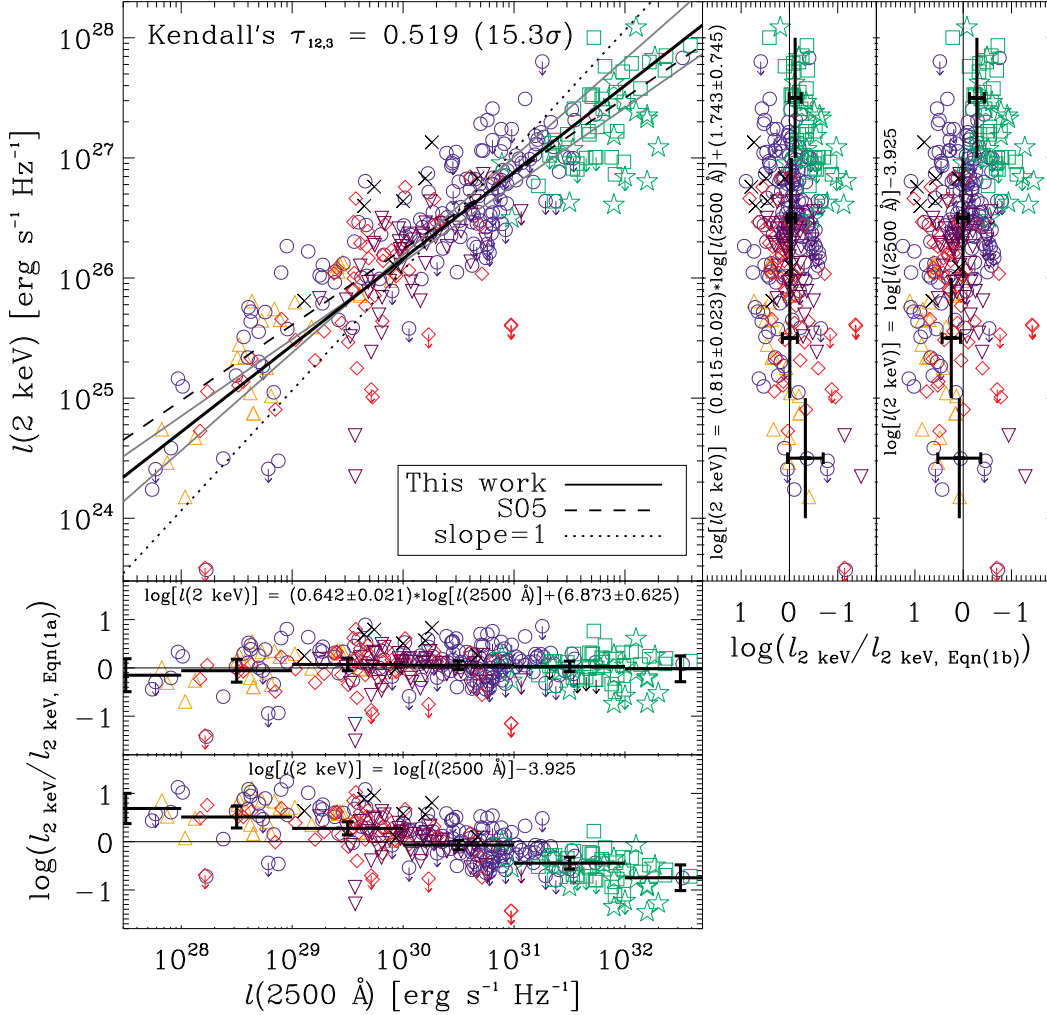


FIG. 4.— (top) Rest-frame 2 keV monochromatic luminosity versus rest-frame 2500 Å monochromatic luminosity. The symmetric, best-fit $l_{2 \text{ keV}} - l_{2500 \text{ Å}}$ relationship, given by Equation (1c), is denoted by a solid, black line. Equations (1a) and (1b) are denoted by solid, gray lines in order of increasing $l_{2 \text{ keV}}$ at $l_{2500 \text{ Å}} = 10^{32} \text{ erg s}^{-1} \text{ Hz}^{-1}$. For comparison, the best-fit line derived by S05 (dashed line) and a $\beta = 1$ relation (dotted line), normalized to best fit the data, are shown. The residuals for Equation (1a) and the $\beta = 1$ relation are shown in the two lower panels, respectively. The residuals for Equation (1b) and the $\beta = 1$ relation are shown in the two panels on the right, respectively. The overlaid error bars denote the mean and the 3σ standard deviation of the mean of the residuals calculated for each $\Delta \log(l_{2500 \text{ Å}}) = 1$ bin. Symbols are defined as in Figure 3, although all symbols are plotted as open to minimize symbol crowding. Limits are denoted with arrows. We find a highly significant (15.3σ) correlation between $l_{2 \text{ keV}}$ and $l_{2500 \text{ Å}}$ (controlling for redshift) with a best-fit slope of $\beta = 0.73 \pm 0.1$, calculated from the ILS bisector.

assumes the residuals are Gaussian distributed). Since both $l_{2 \text{ keV}}$ and $l_{2500 \text{ Å}}$ are observed, neither can be truly called the “independent” or “dependent” variable. Indeed, a different result can be obtained if the residuals of the independent variable are instead minimized [i.e., $\text{OLS}(X | Y)$]. Rather than use the traditional $\text{OLS}(Y | X)$, we choose a method that instead provides a symmetric fit to the data. Following the arguments in § 5 of Isobe et al. (1990), we use the OLS bisector, which simply bisects the two lines from the $\text{OLS}(Y | X)$ and $\text{OLS}(X | Y)$, or in our case $\text{ILS}(Y | X)$ and $\text{ILS}(X | Y)$ from the EM Algorithm in ASURV.

We perform linear regressions with ASURV on the full sample of 333 AGNs and find the relation between $l_{2 \text{ keV}}$ and $l_{2500 \text{ Å}}$ to be

$$\log(l_{2 \text{ keV}}) = (0.64 \pm 0.02) \log(l_{2500 \text{ Å}}) + (6.87 \pm 0.63) \quad (1a)$$

using $\text{ILS}(Y | X)$ (i.e., treating $l_{2 \text{ keV}}$ as the dependent variable) and

$$\log(l_{2 \text{ keV}}) = (0.82 \pm 0.02) \log(l_{2500 \text{ Å}}) + (1.74 \pm 0.75) \quad (1b)$$

using $\text{ILS}(X | Y)$ (i.e., treating $l_{2500 \text{ Å}}$ as the dependent variable). Note that the slope of the $l_{2 \text{ keV}} - l_{2500 \text{ Å}}$ relation does depend on which luminosity is used as the dependent variable, but both cases are inconsistent with $\beta = 1$. We use the equations given in Table 1 of Isobe et al. (1990) to calculate the bisector of the two regression lines. We find the ILS bisector to be

$$\log(l_{2 \text{ keV}}) = (0.72 \pm 0.01) \log(l_{2500 \text{ Å}}) + (4.53 \pm 0.69) \quad (1c)$$

In Figure 4, we show $l_{2 \text{ keV}}$ versus $l_{2500 \text{ Å}}$ for the full AGN sample (top panel). We show the symmetric, best-fit $l_{2 \text{ keV}} - l_{2500 \text{ Å}}$ relationship, given by Equation (1c), as a solid, black

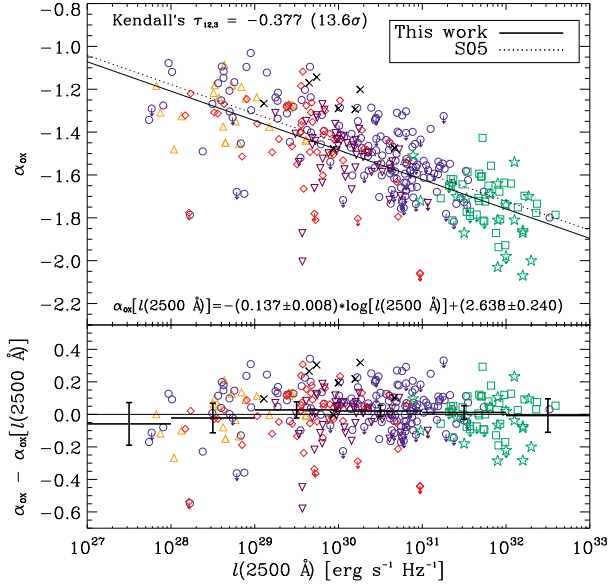


FIG. 5.— (top) α_{OX} vs. rest-frame 2500 Å monochromatic luminosity. The best-fit line from Equation (2) is shown (solid line). For comparison, the best fit line derived by S05 (dotted line) is also shown. (bottom) Residuals from the fit shown in the top panel. The overlaid error bars denote the mean and the 3σ standard deviation of the mean of the residuals calculated for each $\Delta\log(l_{2500\text{Å}}) = 1$ bin. Symbols are defined as in Figure 3, although all symbols are plotted as open to minimize symbol crowding. Limits are denoted with arrows. We find a highly significant (13.6σ) correlation between α_{OX} and $l_{2500\text{Å}}$ (controlling for redshift).

line. Equations (1a) and (1b) are denoted by solid, gray lines in order of increasing $l_{2\text{keV}}$ at $l_{2500\text{Å}} = 10^{32} \text{ erg s}^{-1} \text{ Hz}^{-1}$. For comparison purposes we show the $l_{2\text{keV}} - l_{2500\text{Å}}$ relation found by S05 (dashed line), along with a $\beta = 1$ relation with a normalization chosen to minimize the $l_{2\text{keV}}$ residuals (dotted line). The residuals for Equation (1a) and the fit assuming $\beta = 1$ are given in the bottom panels, with the mean and the (3σ) standard deviation of the mean calculated for sources in each $\Delta\log(l_{2500\text{Å}}) = 1$ bin denoted with large error bars. The residuals for Equation (1b) and the fit assuming $\beta = 1$ are given in the right-hand panels using the same symbols. From the systematic $\beta = 1$ residuals present along both axes, it is apparent that a $\beta = 1$ relation provides an unsatisfactory fit to the data, independent of the luminosity considered as the dependent variable.

3.3. α_{OX} versus $l_{2500\text{Å}}$

Given the highly significant correlation between $l_{2\text{keV}}$ and $l_{2500\text{Å}}$ found for our AGN sample, we investigate how α_{OX} changes with respect to $l_{2500\text{Å}}$, $l_{2\text{keV}}$, and redshift. For our optically-selected AGN sample we confirm a highly significant (13.6σ) anti-correlation between α_{OX} and $l_{2500\text{Å}}$ when controlling for the effects of redshift. The best-fit parameters for the $\alpha_{\text{OX}} - l_{2500\text{Å}}$ relation are

$$\alpha_{\text{OX}} = (-0.137 \pm 0.008) \log(l_{2500\text{Å}}) + (2.638 \pm 0.240) \quad (2)$$

In Figure 5, we show α_{OX} versus $l_{2500\text{Å}}$ for our full AGN sample. We show the best-fit linear regression found for this sample, given in Equation (2), as a solid line. The residuals for the fit are given in the bottom panel, with the mean and standard deviation of the mean calculated for sources in each $\Delta\log(l_{2500\text{Å}}) = 1$ bin denoted with 3σ error bars. For comparison purposes we show the $\alpha_{\text{OX}} - l_{2500\text{Å}}$ relation found by S05 (dotted line).

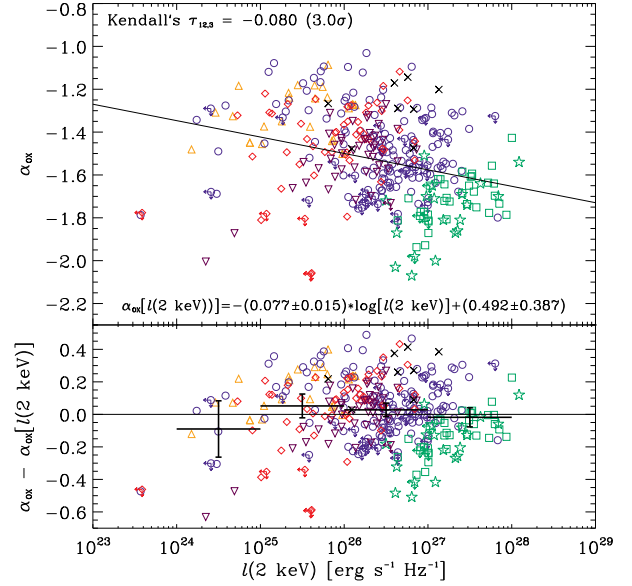


FIG. 6.— (top) α_{OX} vs. rest-frame 2 keV monochromatic luminosity. The best-fit line from Equation (3) is shown (solid line). (bottom) Residuals from the fit shown in the top panel. The overlaid error bars denote the mean and the 3σ standard deviation of the mean of the residuals calculated for each $\Delta\log(l_{2\text{keV}}) = 1$ bin. Symbols are defined as in Figure 3, although all symbols are plotted as open to minimize symbol crowding. Limits are denoted with arrows. We find a lower, but still significant (3.0σ) correlation between α_{OX} and $l_{2\text{keV}}$ (controlling for redshift).

3.4. α_{OX} versus $l_{2\text{keV}}$

The correlation between α_{OX} and $l_{2\text{keV}}$ has been previously examined (Green et al. 1995), but the AGN samples used had low X-ray detection fractions and included both radio-loud AGNs and BALQSOs, both of which can obfuscate the intrinsic X-ray emission of interest here (see § 1). In addition, Green et al. (1995) did not check if the correlation between α_{OX} and $l_{2\text{keV}}$ was the result of a true correlation, or a by-product of the known correlation between $l_{2\text{keV}}$ and redshift.

The high X-ray detection fraction of our AGN sample allows us to examine the correlation between α_{OX} and $l_{2\text{keV}}$. We find a weaker, but still significant (3.0σ) anti-correlation between α_{OX} and $l_{2\text{keV}}$ when controlling for the effects of redshift and taking into account the double-censoring present in this relation (i.e., censoring of both the dependent and independent variables). The linear-regression methods used previously to derive the parameters of the correlations (EM and Buckley-James regression algorithms) are only strictly valid if double-censoring is not present. However, given the high X-ray detection fraction of our sample, we continue to use the aforementioned EM and Buckley-James regression methods, assuming the independent variable ($l_{2\text{keV}}$) is detected. Note that our choice of linear-regression techniques does not affect the significance of the anti-correlation presented above.

The best-fit parameters for the $\alpha_{\text{OX}} - l_{2\text{keV}}$ relation from the EM regression method are

$$\alpha_{\text{OX}} = (-0.077 \pm 0.015) \log(l_{2\text{keV}}) + (0.492 \pm 0.387) \quad (3)$$

In Figure 6, we show α_{OX} versus $l_{2\text{keV}}$ for our full AGN sample; the best-fit linear regression found for this sample, given in Equation (3), is shown by a solid line. The residuals for the fit are given in the bottom panel, with the mean and standard deviation of the mean calculated for sources in each $\Delta\log(l_{2\text{keV}}) = 1$ bin denoted with 3σ error bars.

The clear trend of higher (i.e., less-negative) α_{OX} values

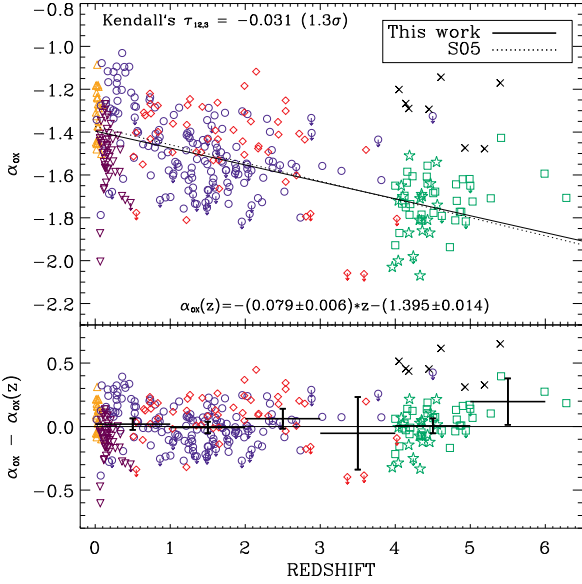


FIG. 7.— (top) α_{OX} vs. redshift. The best-fit line from Equation (4) is shown (solid line). For comparison, the best-fit line derived by S05 (dotted line) is also shown. (bottom) Residuals from the fit shown in the top panel. The overlaid error bars denote the mean and the 3σ standard deviation of the mean of the residuals calculated for each $\Delta z = 1$ bin. Symbols are defined as in Figure 3, although all symbols are plotted as open to minimize symbol crowding. Limits are denoted with arrows. We find no significant (1.3σ) correlation between α_{OX} and redshift (controlling for $l_{2500\text{\AA}}$).

with decreasing $l_{2500\text{\AA}}$ seen in Fig 5 is not as apparent in the $\alpha_{\text{OX}} - l_{2\text{keV}}$ plot. This could be due, in part, to the smaller range in X-ray luminosity covered by the AGNs ($\Delta \log(l_{2\text{keV}}) = 4$) compared to the UV luminosity range ($\Delta \log(l_{2500\text{\AA}}) = 5$). In addition, the scatter in the residuals for the $\alpha_{\text{OX}} - l_{2\text{keV}}$ relation is larger than that seen for $l_{2500\text{\AA}}$.

3.5. α_{OX} versus redshift

To test for a possible redshift dependence of α_{OX} we measure the partial correlation of α_{OX} and z , controlling for $l_{2500\text{\AA}}$. We do not find a significant correlation between α_{OX} and redshift (1.3σ), consistent with previous α_{OX} studies. The best-fit parameters for the $\alpha_{\text{OX}} - z$ relation are

$$\alpha_{\text{OX}} = (-0.079 \pm 0.006) z - (1.395 \pm 0.014) \quad (4)$$

In Figure 7, we show α_{OX} versus z for our full AGN sample. We show the best-fit linear regression found for this sample, given in Equation (4), as a solid line. The apparent correlation between α_{OX} and redshift is simply an artifact of the $l_{2500\text{\AA}} - z$ correlation. The residuals for the fit are given in the bottom panel, with the mean and standard deviation of the mean calculated for sources in each $\Delta z = 1$ bin denoted with 3σ error bars. For comparison purposes we show the $\alpha_{\text{OX}} - z$ relation found by S05 (dotted line).

In Figure 8, we show the $\alpha_{\text{OX}} - \alpha_{\text{OX}}(l_{2500\text{\AA}})$ residuals as a function of redshift (top panel) and the $\alpha_{\text{OX}} - \alpha_{\text{OX}}(z)$ residuals as a function of $l_{2500\text{\AA}}$ (bottom panel). It is clear from Figure 8 that there is a strong luminosity dependence in the $\alpha_{\text{OX}} - \alpha_{\text{OX}}(z)$ residuals, while the $\alpha_{\text{OX}} - \alpha_{\text{OX}}(l_{2500\text{\AA}})$ residuals show no strong redshift dependence. Using ASURV to find α_{OX} as a function of both $l_{2500\text{\AA}}$ and redshift, we find the following relation.

$$\alpha_{\text{OX}} = (-0.126 \pm 0.013) \log(l_{2500\text{\AA}}) - (0.010 \pm 0.009) z + (2.311 \pm 0.372) \quad (5)$$

Equation (5) shows that the coefficient of z is statistically consistent with zero (1.1σ), which agrees with the findings of S05 and is consistent with α_{OX} being independent of redshift.

We use the $\alpha_{\text{OX}} - \alpha_{\text{OX}}(l_{2500\text{\AA}})$ residuals to constrain the maximum possible residual dependence of α_{OX} on redshift, which constrains the maximum amount the ratio of the UV-to-X-ray luminosity can evolve with redshift. We find the best-fit parameters of the residuals to be $\langle \alpha_{\text{OX}} - \alpha_{\text{OX}}(l_{2500\text{\AA}}) \rangle = (-0.004 \pm 0.006) z - (0.004 \pm 0.012)$. The maximum absolute 1σ value for the slope of the residuals is $0.010 z$, which at $z = 5$ is equal to 0.05 . The ratio between the UV and X-ray flux is, by definition, $r = f_{\nu}(2500\text{\AA})/f_{\nu}(2\text{keV}) = 10^{2.606\alpha_{\text{OX}}}$. Differentiating with respect to α_{OX} , we get $\delta r/r = 2.606 \ln(10) \delta \alpha_{\text{OX}} \simeq 6 \delta \alpha_{\text{OX}} \simeq 0.30$, for $\delta \alpha_{\text{OX}} = 0.05$. Thus the ratio of UV-to-X-ray flux has not changed by more than 30% (1σ) over the redshift range $z = 0 - 5$.

To examine if α_{OX} is independent of redshift over the range of luminosities observed, we divided the AGNs equally into three luminosity bins, with each bin containing 111 sources. We plot the $\alpha_{\text{OX}} - \alpha_{\text{OX}}(l_{2500\text{\AA}})$ residuals as a function of redshift for each UV luminosity bin in Figure 9. It is apparent that the COMBO-17 sample and the Seyfert 1 sample of S05 comprise most of the lower-luminosity AGNs ($\log(l_{2500\text{\AA}}) < 29.812$). The number of COMBO-17 AGNs decreases in the moderate UV luminosity bin where the BQS and SDSS AGNs become prevalent ($27.812 < \log(l_{2500\text{\AA}}) < 30.795$). At the highest luminosities, the $z > 4$ AGNs and the SDSS sample dominate ($\log(l_{2500\text{\AA}}) > 30.795$). None of the residuals shows any indications of having a systematic offset, showing that AGNs spanning five decades in UV luminosity show little α_{OX} evolution with redshift.

3.6. Comparing $\alpha_{\text{OX}} - z$ and $l_{2\text{keV}} - z$ relations

Recent discussions have questioned the validity of measuring the redshift evolution of α_{OX} controlling for the effects of

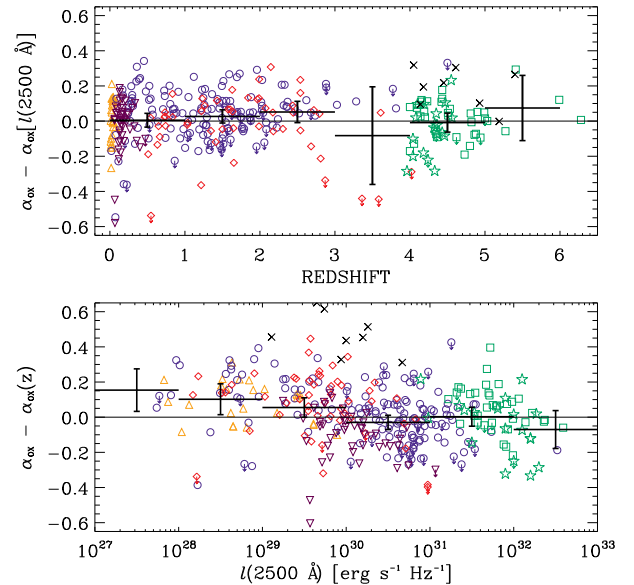


FIG. 8.— α_{OX} residuals as a function of redshift (top panel) and $l_{2500\text{\AA}}$ (bottom panel). The overlaid error bars denote the mean and the 3σ standard deviation of the mean of the residuals calculated for each $\Delta z = 1$ bin (top panel) or $\Delta \log(l_{2500\text{\AA}}) = 1$ bin (bottom panel). Symbols are defined as in Figure 3, although all symbols are plotted as open to minimize symbol crowding. Limits are denoted with arrows. The systematic residuals in the lower plot indicate that α_{OX} cannot be dependent on redshift alone.

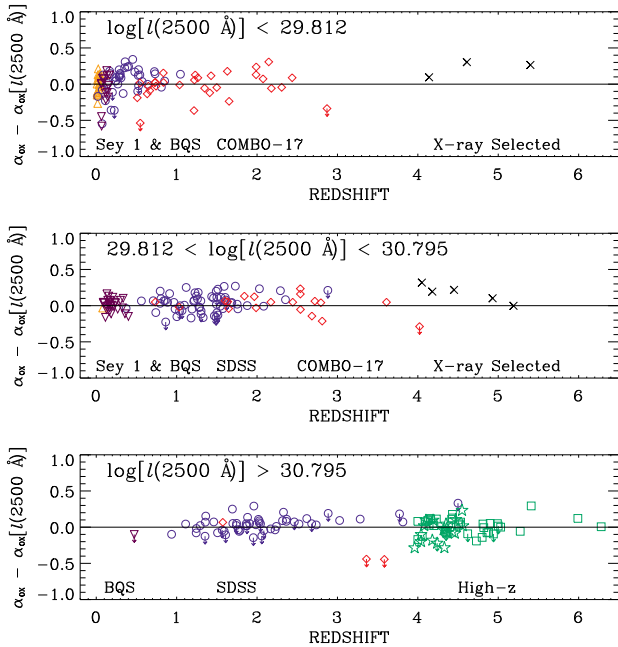


FIG. 9.— α_{ox} residuals as a function of redshift shown for three luminosity ranges. Symbols are defined as in Figure 3, although all symbols are plotted as open to minimize symbol crowding. Limits are denoted with arrows. There is no apparent redshift dependence of the $\alpha_{\text{ox}} - \alpha_{\text{ox}}(l_{2500 \text{ \AA}})$ residuals within any luminosity range.

$l_{2500 \text{ \AA}}$, since $l_{2500 \text{ \AA}}$ and α_{ox} are, by construction, correlated (B. Kelly 2005, personal communication). It has been suggested that measuring the redshift evolution of $l_{2 \text{ keV}}$, controlling for $l_{2500 \text{ \AA}}$, is a better measure of the evolution of α_{ox} since this relation does not include the aforementioned $\alpha_{\text{ox}} - l_{2500 \text{ \AA}}$ correlation. However, it is not clear that the redshift evolution of $l_{2 \text{ keV}}$ and α_{ox} are necessarily related, even when controlling for the effects of $l_{2500 \text{ \AA}}$ (e.g., M. Akritas 2005, personal communication). We examine the redshift evolution of $l_{2 \text{ keV}}$ using our sample and find a highly significant partial correlation between $l_{2 \text{ keV}} - z$, controlling for $l_{2500 \text{ \AA}}$ ($\tau_{12,3} = 0.21$, $\sigma = 8.7$). If the $l_{2 \text{ keV}} - z$ partial correlation is indeed a proxy for $\alpha_{\text{ox}} - z$, then this result conflicts with our finding in §3.5 that α_{ox} does not evolve with redshift. We examine this apparent paradox further using both Monte Carlo simulations and a subset of our full data sample that better covers the $l_{2500 \text{ \AA}} - z$ plane.

To determine if the $l_{2 \text{ keV}} - z$ correlation is real or fake, we ran a set of simulations designed to assess the strength of partial correlations expected for samples with similar $l_{2500 \text{ \AA}} - z$ distributions. We started by randomly assigning an $l_{2500 \text{ \AA}}$ value in the observed range ($29.0 < l_{2500 \text{ \AA}} < 32.5$) to each AGN in our sample. We then computed $l_{2 \text{ keV}}$ for each source assuming the ILS bisector relation in Equation 1c, including a random scatter comparable to that observed. We compute the $l_{2 \text{ keV}} - z$ partial correlation (controlling for $l_{2500 \text{ \AA}}$) for ten random samples to obtain an average value for the strength and significance of the partial correlation. In these realizations there is no $l_{2500 \text{ \AA}} - z$ dependence, by construction. We find average correlation strength of $\tau_{12,3} = 0.06 \pm 0.02$ with $\sigma = 2.2 \pm 0.7$, significantly lower than for our actual sample. However, if we instead constrain the random $l_{2500 \text{ \AA}}$ to follow the observed $l_{2500 \text{ \AA}} - z$ dependence, the partial tau method finds a more significant, *but false*, partial correlation of $\tau_{12,3} = 0.17 \pm 0.01$ with $\sigma = 7.0 \pm 0.5$. These simulations suggest that the strength of the correlation between

$l_{2 \text{ keV}}$ and redshift is an artifact of the strong $l_{2500 \text{ \AA}} - z$ relation in flux-limited samples. While the partial-correlation methods of Kendall’s tau are designed to remove the contribution of the third variable (in this case $l_{2500 \text{ \AA}}$) from the measurement of the correlation between the first and second variables ($l_{2 \text{ keV}}$ and z), when the correlations between the controlling variable and the first and/or second variable are very strong, apparently significant, but false, partial correlations can arise.

To test further the $l_{2 \text{ keV}} - z$ relation, we limit our analysis to sources with $29.3 < l_{2500 \text{ \AA}} < 31$ and $z < 3$, consisting of 187 sources (see the subsample box in Figure 3). This subsample more completely fills the $l_{2500 \text{ \AA}} - z$ plane and thus is less affected by the strong $l_{2500 \text{ \AA}} - z$ correlation present in flux-limited samples. Using this subsample, we find $l_{2 \text{ keV}} - z$ partial-correlation results of $\tau_{12,3} = 0.11$ with $\sigma = 2.8$, again showing that the strength of the relation diminishes greatly when the flux-limited nature of the sample is reduced or eliminated. For comparison, the $\alpha_{\text{ox}} - l_{2500 \text{ \AA}}$ partial correlation decreases, as one would expect from the smaller sample size and reduced $l_{2500 \text{ \AA}}$ and z range, but it remains significant ($\tau_{12,3} = -0.29$, $\sigma = 7.0$). From these tests it is apparent that the redshift evolution of $l_{2 \text{ keV}}$ is strongly influenced by the strong correlation between $l_{2500 \text{ \AA}}$ and z and thus should not be used as a substitute for the $\alpha_{\text{ox}} - z$ relation.

3.7. Investigating non-linear α_{ox} correlations

From the previous three sections it is clear that α_{ox} is most significantly correlated with $l_{2500 \text{ \AA}}$, but does the slope of this correlation remain the same over the entire range of UV luminosities, or is the $\alpha_{\text{ox}} - l_{2500 \text{ \AA}}$ relation non-linear? From Figure 4 it appears possible that the $l_{2 \text{ keV}} - l_{2500 \text{ \AA}}$ slope may become steeper at lower luminosities. It is difficult to tell from the plot, however, as lower-luminosity sources typically have larger measurement errors. Non-linearity may also be hinted at in the residual plot in Figure 5. While all of the 3σ error bars for the mean residuals in each luminosity bin are consistent with zero, there is a slight curve seen in the mean residuals, peaking around $10^{30} \text{ erg s}^{-1} \text{ Hz}^{-1}$.

We investigate this potential change in the slope of the $\alpha_{\text{ox}} - l_{2500 \text{ \AA}}$ relation by dividing the sample in half using the median UV luminosity ($\log(l_{2500 \text{ \AA}}) = 30.352$) and calculating the slope of the best-fit line for both the high-luminosity and low-luminosity halves of the sample. We find the coefficient for the low-luminosity half to be flatter (-0.098 ± 0.019) than for the high-luminosity half (-0.152 ± 0.019). We use Student’s t-test to determine if these two slopes are drawn from the same distribution. We find only a 5% probability that the best-fit slopes for the high and low-luminosity halves of the distribution are drawn from the same parent distribution, suggesting that the slope of the $\alpha_{\text{ox}} - l_{2500 \text{ \AA}}$ relation may be $l_{2500 \text{ \AA}}$ dependent.

We use this same method to determine if the $\alpha_{\text{ox}} - l_{2500 \text{ \AA}}$ slope is dependent on redshift. We divide the full sample into low-redshift ($z \leq 2$) and high-redshift ($z > 2$) subsamples, containing 230 and 103 sources, respectively. We do not find a significant difference in the best-fit slopes for the low-redshift (-0.125 ± 0.012) and high-redshift (-0.147 ± 0.020) subsamples. Using Student’s t-test, we find a 37% chance that the slopes of the low-redshift and high-redshift subsamples are drawn from the same parent distribution.

4. DISCUSSION AND CONCLUSIONS

4.1. Summary of AGN Sample

In this paper, we examine the correlations between $l_{2500 \text{ \AA}}$, $l_{2 \text{ keV}}$, α_{ox} , and redshift for optically-selected AGNs. We extend the coverage of the luminosity-redshift plane relative to the S05 sample by adding 52 lower-luminosity AGNs discovered by the COMBO-17 survey, 46 high-luminosity, low-redshift ($z < 0.5$) AGNs from the BQS, and 19 high-redshift ($z > 4$) AGNs from recently published, targeted X-ray/optical AGN studies. Radio-loud AGNs and BALQSOs are excluded from our sample whenever possible, and the effects of host-galaxy contamination are largely removed for the COMBO-17 AGNs using high-resolution ACS observations. These additional AGNs bring the total sample to 333 optically-selected AGNs, 293 (88%) of which have detected X-ray counterparts.

In Table 5 we present the statistical properties of the full sample, broken into $\Delta \log(l_{2500 \text{ \AA}}) = 1$ bins. The Kaplan-Meier estimator within ASURV was used to calculate the statistical properties of the sources in each bin. The redshift range, mean, RMS error, median, and both 25th and 75th percentile values are given, along with the value of $l_{2500 \text{ \AA}}$ and α_{ox} calculated from Equations (1c) and (2), respectively, using the mean $l_{2500 \text{ \AA}}$ value given in the appropriate bin. This table also gives both the expected value of $l_{2 \text{ keV}}$ and α_{ox} for each $\Delta \log(l_{2500 \text{ \AA}}) = 1$ bin as well as the spread around the expectation values. From the table, it appears that the spread of $l_{2 \text{ keV}}$ decreases with increasing $l_{2500 \text{ \AA}}$ for the bins with statistically significant numbers of sources. There is no clear $l_{2500 \text{ \AA}}$ dependence on the spread of α_{ox} . This table is useful in identifying AGNs that may be X-ray weak or assessing the excess associated with jet-linked X-ray emission.

4.2. Results of Partial Correlation Analyses

To measure correlations in our data we employ partial-correlation methods that deal with censored data. We confirm that the monochromatic 2500 \AA and 2 keV luminosities are highly correlated (15.3σ), considering the effects of redshift, and follow the relation $l_{2 \text{ keV}} \propto l_{2500 \text{ \AA}}^\beta$, where $\beta = 0.73 \pm 0.01$ (from the ILS bisector), and not $\beta = 1$ as found in some previous studies.

We investigate how the ratio of the X-ray and UV luminosities, α_{ox} , is correlated with $l_{2500 \text{ \AA}}$, $l_{2 \text{ keV}}$, and redshift for our AGN sample. When taking into account the effects of redshift, we confirm that the $\alpha_{\text{ox}} - l_{2500 \text{ \AA}}$ anti-correlation is highly significant (13.6σ) but find a much smaller, but still significant, anti-correlation for the $\alpha_{\text{ox}} - l_{2 \text{ keV}}$ relation (3.0σ). The discrepancy in the significance of these two correlations is due, in part, to the slope of the $l_{2 \text{ keV}} - l_{2500 \text{ \AA}}$ relation being less than unity. As can be seen in Figure 4, the range of possible values of $l_{2 \text{ keV}}$ for a given value of $l_{2500 \text{ \AA}}$ is smaller (and hence the range of α_{ox} values is smaller) than the range of possible values of $l_{2500 \text{ \AA}}$ for a given value of $l_{2 \text{ keV}}$. In addition, some AGNs are more variable in the X-ray than they are in the optical/UV, with long-timescale X-ray observations of Seyfert 1s showing variability $\geq 100\%$ for some sources (Uttley & McHardy 2004, and references therein), which increases the possible ranges of $l_{2 \text{ keV}}$ even more dramatically for a given value of $l_{2500 \text{ \AA}}$.

Our analysis did not reveal any significant (1.3σ) evolution of α_{ox} with redshift (when considering the effects of $l_{2500 \text{ \AA}}$), which is consistent with the majority of previous α_{ox} studies. However, including the COMBO-17 AGNs in

TABLE 4
PARTIAL CORRELATION RESULTS.

Relation	Controlling Variable	Kendall's $\tau_{12,3}$	Significance
Total Sample			
$l_{2 \text{ keV}}$ vs. $l_{2500 \text{ \AA}}$	z	0.519	15.3σ
α_{ox} vs. $l_{2500 \text{ \AA}}$	z	-0.377	13.6σ
α_{ox} vs. $l_{2 \text{ keV}}$	z	-0.080	3.0σ
α_{ox} vs. z	$l_{2500 \text{ \AA}}$	-0.031	1.3σ
Removed COMBO-17 AGNs with $\Gamma < 1.6$			
$l_{2 \text{ keV}}$ vs. $l_{2500 \text{ \AA}}$	z	0.505	13.7σ
α_{ox} vs. $l_{2500 \text{ \AA}}$	z	-0.396	13.7σ
α_{ox} vs. $l_{2 \text{ keV}}$	z	-0.079	3.0σ
α_{ox} vs. z	$l_{2500 \text{ \AA}}$	-0.004	0.2σ

NOTE. — Kendall's partial-rank correlation is defined as $\tau_{12,3} = \frac{\tau_{12} - \tau_{13}\tau_{23}}{[(1 - \tau_{13}^2)(1 - \tau_{23}^2)]^{1/2}}$, where τ_{xy} is the Kendall rank-correlation coefficient between data vectors x and y (Akritas & Siebert 1996).

our study allows us to constrain, for the first time, the spectral evolution of moderate-luminosity AGNs out to high redshifts. Since moderate-luminosity AGNs are the numerically dominant type of AGN in the Universe, and X-ray surveys have found luminosity-dependent density evolution for such AGNs, it is important to understand the spectral evolution of these types of sources. The lack of cosmic evolution of α_{ox} also suggests that the energy generation mechanisms that create AGN emission locally are already in place at $z \simeq 5 - 6$. This agrees with AGN studies which find no significant evolution in the continuum shape of AGNs at high-redshifts from radio (e.g., Petric et al. 2003), optical/UV (e.g., Pentericci et al. 2003), and X-ray (e.g., Page et al. 2005; Shemmer et al. 2005) studies.

4.3. Comparison with X-ray-Selected, $z > 4$ AGNs

In §3, we limited our analyses and discussion to the 333 optically-selected AGNs in our sample. Here we determine if the relations we derived for $l_{2500 \text{ \AA}}$, $l_{2 \text{ keV}}$, α_{ox} , and redshift also hold for the eight published X-ray-selected, radio-quiet, $z > 4$ AGNs (see §2.2.3). While subject to different selection biases than our main AGN sample, these X-ray-selected AGNs substantially extend the coverage of the luminosity - redshift plane (see crosses in Figure 3a), and thus they can be useful in determining if the aforementioned relations are also valid for high-redshift, low-luminosity AGNs.

From Figures 4, 5, and 6 it is apparent that the X-ray-selected AGNs, while considerably fainter in $l_{2500 \text{ \AA}}$ than the optically-selected AGNs in our sample at similar redshifts, have α_{ox} values that do not significantly stand out from the α_{ox} values of the optically-selected AGNs. While the X-ray-selected AGNs do populate the high (less-negative) portion of the α_{ox} distributions in Figures 5 and 6, this is not unexpected because X-ray selection is biased toward sources that are X-ray bright. In other words, for a group of sources at a given $l_{2500 \text{ \AA}}$ with the observed spread in α_{ox} , X-ray surveys are biased toward selecting those sources with higher α_{ox} values (i.e., the AGNs that are relatively brighter in X-rays).

In Figure 7, the X-ray-selected sources all lie well above the best-fit $\alpha_{\text{ox}} - z$ relation derived from our main sample. This apparent discrepancy is expected if α_{ox} is indeed dependent on $l_{2500 \text{ \AA}}$ and not z . The eight X-ray-selected AGNs

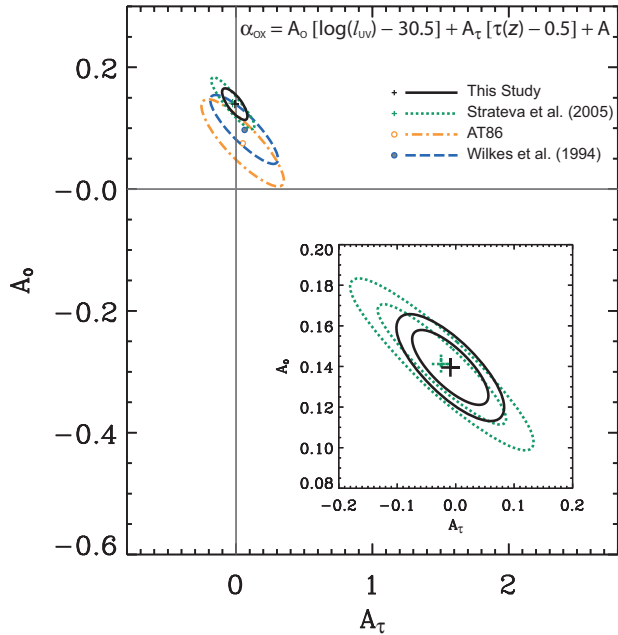


FIG. 10.— Best-fit values and $\Delta S = 4.61$ (90%) confidence contours for the coefficients A_0 and A_τ for our sample (black cross, solid black contour), the sample of S05 (green cross, dotted green contour), and the samples examined by Avni & Tananbaum (1986) (open orange circle, dot-dashed orange contour) and Wilkes et al. (1994) (filled blue circle, dashed blue contour). Inset: A magnified view of the contours for our sample. Both the 68% ($\Delta S = 2.30$) and 90% ($\Delta S = 4.61$) confidence contours (solid black contours) are shown. For comparison, the 68% and 90% confidence contours of the S05 sample are also shown (dotted green contours).

have considerably smaller $l_{2500 \text{ \AA}}$ values than the optically selected, $z > 4$ AGNs, and thus we would predict that they would have higher (less negative) values of α_{OX} from Equation (2). Indeed, the α_{OX} residuals shown in Figures 8 and 9 demonstrate that the X-ray-selected AGNs (crosses) agree fairly well with our conclusion that α_{OX} is dependent on $l_{2500 \text{ \AA}}$ and shows no significant redshift dependence. To test further this conclusion we again ran the partial correlations described in §3, this time including the eight X-ray-selected sources. We find that the significance of most of the correlations presented in Table 4 increase $\sim 0.3 - 0.8\sigma$. The $\alpha_{\text{OX}} - z$ partial correlation increases by $\sim 0.7\sigma$, but it is still below the threshold of a significant correlation. In addition, while the X-ray-selected AGNs do increase the coverage of the luminosity - redshift plane, it is not clear what effect the different selection biases of the X-ray-selected AGNs will have on these correlations.

4.4. Comparison with Earlier Studies

The AGN sample presented here enables us to provide the tightest constraints to date on the contributions of $l_{2500 \text{ \AA}}$ and redshift to α_{OX} . To illustrate our improvement over some past studies, we compare our results with those of Avni & Tananbaum (1986, hereafter AT86), Wilkes et al. (1994), and S05. Note that the first two authors use cosmological look-back time, $\tau(z)$, in units of the present age of the Universe, and not redshift in their calculations. We calculate $\tau(z)$ for our sources and use the method outlined in §§ 3 and 4 of AT86 to calculate confidence contours. We rename A_z from AT86 to A_τ since, strictly speaking, it is the coefficient of cosmological look-back time which is not a linear function of redshift.

This modification changes Equation (6) of AT86¹⁰ to

$$\bar{\alpha}_{\text{OX}}(l_{2500 \text{ \AA}}, z | \text{X-ray Loud}) = A_0 [\log(l_{2500 \text{ \AA}}) - 30.5] + A_\tau [\tau(z) - 0.5] + A \quad (6)$$

For our sample, we find best-fit values of $[A_0, A_\tau, A] = [0.140_{-0.016}^{+0.011}, -0.009_{-0.040}^{+0.055}, 1.553 \pm 0.014]$ for Equation 6. In Figure 10, we show the $\Delta S = 4.61$ confidence contours for our data and the samples presented in AT86, Wilkes et al. (1994), and S05. These are equivalent to 90% confidence contours taking two parameters to be of interest. The tighter constraints provided by our data have a number of sources. Our X-ray detection fraction (88%) is higher than either AT86 (61%) or Wilkes et al. (1994) (64%). Unlike early AGN samples used to study α_{OX} , our data represent a relatively homogeneous collection of AGNs where we attempted to remove or reduce sources of systematic errors (radio jets, absorption, galaxy contribution, etc.). Finally, to our knowledge, our AGN sample provides the best coverage of the luminosity - redshift plane to date.

4.5. Comparing X-ray and Optical AGN Luminosity Functions

Understanding the relationship between $l_{2 \text{ keV}}$ and $l_{2500 \text{ \AA}}$ in AGNs aids in explaining discrepancies between the AGN X-ray and optical luminosity functions (XLF and OLF, respectively). For luminous AGNs, both the OLF (e.g., Boyle et al. 2000; Croom et al. 2004; Richards et al. 2005, 2006) and XLF (e.g., Cowie et al. 2003; Ueda et al. 2003; Barger et al. 2005; Hasinger et al. 2005; La Franca et al. 2005) are consistent with pure luminosity evolution (PLE), with the peak activity of luminous AGNs occurring at $z = 2 - 3$. However, recent X-ray surveys have found that low-luminosity ($L_{2-8 \text{ keV}} \lesssim 10^{44} \text{ erg s}^{-1}$) AGNs do not agree with the PLE model, but instead appear to undergo luminosity-dependent density evolution (LDDE; e.g., Ueda et al. 2003; Steffen et al. 2003; Barger et al. 2005; Hasinger et al. 2005; La Franca et al. 2005; Silverman et al. 2005a). These studies found that the peak density of low-luminosity AGNs occurs at lower redshifts than for high-luminosity AGNs, an example of “cosmic-downsizing”. LDDE is not seen in deep optical AGN surveys where the OLFs of low-luminosity AGNs are not well constrained and are consistent with both PLE and pure density evolution (PDE) models (Wolf et al. 2003).

Given that AGNs found in deep X-ray-selected samples appear to undergo LDDE, does this necessitate LDDE for optically-selected samples as well? We can use the LDDE equations given in § 5.2 of Ueda et al. (2003, hereafter U03) and the relationship between $l_{2 \text{ keV}}$ and $l_{2500 \text{ \AA}}$ we find for optically-selected AGNs (Equation 1c) to examine how the LDDE parameters change if the optical luminosity is substituted for the X-ray luminosity. Equations (16) and (17) of U03 give the evolution factor, $e(L_X, z)$, as a function of both the luminosity and redshift, which is unique to LDDE models (for PLE and PDE, the evolution factor only depends upon redshift). More specifically, the redshift cutoff, z_c , included in the evolution factor is a function of luminosity in LDDE models and is a constant in PLE and PDE models. Applying our $l_{2 \text{ keV}} - l_{2500 \text{ \AA}}$ relation to the redshift cutoff (Equation 17 of U03), we find that the power-law index, α , becomes $\alpha' = \alpha \cdot \beta$, where β is the slope of the $l_{2 \text{ keV}} - l_{2500 \text{ \AA}}$ relation,

¹⁰ In AT86, α_{OX} is defined to be positive. Thus, the coefficients A_0 and A_τ have the opposite sign as the coefficients presented the previous equations.

TABLE 5
SAMPLE STATISTICS

$\log(l_{2500 \text{ \AA}})$ Range	27 – 28	28 – 29	29 – 30	30 – 31	31 – 32	32 – 33
Number of Sources	6	41	84	121	67	14
Number of X-ray Detections	5	38	82	99	55	14
X-ray Detection Fraction	83%	93%	98%	82%	82%	100%
Redshift Range	0.009 – 0.201	0.009 – 1.264	0.033 – 2.870	0.085 – 4.190	0.472 – 6.280	2.736 – 4.550
$\log(l_{2500 \text{ \AA}})$						
Mean $\log(l_{2500 \text{ \AA}})$	27.847	28.604	29.622	30.540	31.552	32.259
RMS $\log(l_{2500 \text{ \AA}})$	0.081	0.250	0.238	0.286	0.292	0.150
25th Percentile	27.753	28.508	29.453	30.283	31.264	32.120
Median $\log(l_{2500 \text{ \AA}})$	27.825	28.630	29.625	30.609	31.523	32.200
75th Percentile	27.890	28.781	29.806	30.791	31.742	32.330
$\log(l_2 \text{ keV})$						
Mean $\log(l_2 \text{ keV})$	24.571	25.149	25.953	26.472 ^a	27.105 ^a	27.600
RMS $\log(l_2 \text{ keV})$	0.318	0.621	0.431	0.418	0.333	0.348
25th Percentile	... ^b	24.873	25.792	26.296	26.879	27.340
Median $\log(l_2 \text{ keV})$	24.463	25.222	26.018	26.462	27.065	27.730
75th Percentile	24.661	25.622	26.221	26.746	27.337	27.836
Value from Equation (1c)	24.749	25.235	25.889	26.478	27.128	27.582
α_{ox}						
Mean α_{ox}	-1.253	-1.322	-1.408	-1.568 ^a	-1.708	-1.788
RMS α_{ox}	0.093	0.192	0.165	0.198	0.146	0.131
25th Percentile	-1.343	-1.451	-1.493	-1.657	-1.810	-1.865
Median α_{ox}	-1.309	-1.291	-1.402	-1.547	-1.691	-1.786
75th Percentile	-1.230	-1.184	-1.289	-1.455	-1.609	-1.717
Value from Equation (2)	-1.189	-1.293	-1.433	-1.559	-1.699	-1.796

^aASURV changed first datum in bin from a censored point to a detection — mean estimate is biased.

^bNo value is reported due to bias by the upper limit and the small number of sources in this bin.

when the X-ray luminosity is replaced with the optical/UV luminosity. The evolution factor becomes independent of optical/UV luminosity [i.e., $e(L_{UV}, z) \rightarrow e(z)$] only when the X-ray and optical/UV emission in AGNs are independent of one another (i.e., $\beta = 0$). Thus, aside from this special case, the LDDE observed for X-ray AGN samples implies LDDE for optical AGN samples.

The $\beta = 0.725$ slope found for the $l_{2500 \text{ \AA}} - l_2 \text{ keV}$ relation (Equation 1c) evinces that a group of AGNs will span a larger range in UV luminosity than in X-ray luminosity. In other words, optical/UV surveys must cover a larger luminosity range than X-ray surveys to probe the same AGN populations. This is apparent when comparing the sky densities of AGNs from deep X-ray and optical surveys (see § 1). The deep X-ray surveys find about an order of magnitude more AGNs per square degree than the deepest optical surveys. Some of this discrepancy is attributable to different AGN selection effects between the X-ray and optical surveys. Host-galaxy contamination is much more prevalent in the optical regime, as is intrinsic obscuration. However, if we compare the depth probed by the optical and X-ray surveys we see that the optical surveys are missing the low-luminosity AGNs that do not fit into the PLE paradigm. Studies of the XLF find the densities of AGNs with $L_{2-8 \text{ keV}} = 10^{42} - 10^{44} \text{ erg s}^{-1}$ peak at lower redshifts than their more luminous cousins, a strong indication of LDDE. This range in hard X-ray luminosity corresponds to a monochromatic $l_2 \text{ keV}$ range of $\log(l_2 \text{ keV}) = 23.9 - 25.9$, assuming $\Gamma = 2$. Using Equation (1c), we find the corresponding monochromatic $l_{2500 \text{ \AA}}$ range to be $\log(l_{2500 \text{ \AA}}) = 26.9 - 29.7$. From Figure 3a it is apparent that the optically-selected AGN samples do not extend to faint enough UV luminosities to detect all of these

AGNs. Even if we assume $\beta = 1$, we find that the optical surveys are still too shallow, but the problem becomes less severe. Assuming $\beta = 1$, the range of $l_2 \text{ keV}$ covered by the X-ray selected AGN surveys corresponds to a monochromatic $l_{2500 \text{ \AA}}$ range of $\log(l_{2500 \text{ \AA}}) = 27.8 - 29.8$, an order of magnitude higher than we get with $\beta = 0.73$. In light of this comparison it is not surprising that LDDE is not required to describe the evolution of the OLF, because optical surveys are not deep enough to probe the AGN luminosities where LDDE becomes apparent in XLF studies.

4.6. Future Studies

This study presents the highest significance $\alpha_{\text{ox}} - l_{2500 \text{ \AA}}$ correlations to date, but significant work remains to be done. The significance of the measured correlations could be substantially improved by eliminating the intrinsic scatter in our data due to UV and X-ray variability. This could be accomplished with concurrent UV and X-ray observations of AGNs with, e.g., *XMM-Newton*. This study could also be extended by including more of the most optically luminous quasars known at $z \sim 1 - 4$. The high luminosities of these quasars make them visible at all redshifts, and their inclusion would reduce the paucity of these sources at low-to-moderate redshifts in our current sample. We could also extend our study to include Low Ionization Nuclear Emission-line Regions (LINERs). These low-luminosity AGNs could better constrain the $\alpha_{\text{ox}} - l_{2500 \text{ \AA}}$ relation, and the additional $l_{2500 \text{ \AA}}$ “leverage” at low luminosities would help test the possible non-linear $\alpha_{\text{ox}} - l_{2500 \text{ \AA}}$ relation suggested by our data. To measure the AGN emission in LINERs it is essential to minimize the contamination from the host galaxy. To do this, the high-resolution capabilities of *HST* and *Chandra* are needed to isolate the intrinsic

AGN emission within LINERs. Finally, there are currently no compelling physical models that explain the origin of the observed $\alpha_{\text{ox}} - l_{2500 \text{ \AA}}$ relation. Any theoretical model attempting to describe the emission mechanisms within AGNs must be able to reproduce this observed relation. There is hope that attempts to model the environments around accreting SMBHs from first principles using relativistic magneto-hydrodynamic simulations (e.g., Hawley et al. 1995; De Villiers & Hawley 2003; Krolik et al. 2005) will be able to explain the observed $\alpha_{\text{ox}} - l_{2500 \text{ \AA}}$ relation, but to our knowledge these simulations have not yet found a physical explanation for the observed $\alpha_{\text{ox}} - l_{2500 \text{ \AA}}$ relation.

We thank the anonymous referee for helpful comments that improved the manuscript. We thank Wolfgang Voges and Thomas Bolter for supplying the 0.5 – 2 keV *ROSAT* count rates for the RASS BQS sample along with Michael Akritas, Ohad Shemmer, and Brandon Kelly for helpful discussions. We gratefully acknowledge support from NSF CAREER award AST-9983783 (A. T. S. and W. N. B.), CXC grant GO4-5157A (A. T. S., W. N. B., B. D. L., and D. P. S.), NASA LTSA grant NAG5-13035 (I. S. and W. N. B.), the

Royal Society (D. M. A), and MIUR COFIN grant 03-02-23 (C. V.)

Funding for the creation and distribution of the SDSS Archive has been provided by the Alfred P. Sloan Foundation, the Participating Institutions, the National Aeronautics and Space Administration, the National Science Foundation, the U.S. Department of Energy, the Japanese Monbukagakusho, and the Max Planck Society. The SDSS Web site is <http://www.sdss.org/>.

The SDSS is managed by the Astrophysical Research Consortium (ARC) for the Participating Institutions. The Participating Institutions are The University of Chicago, Fermilab, the Institute for Advanced Study, the Japan Participation Group, The Johns Hopkins University, the Korean Scientist Group, Los Alamos National Laboratory, the Max-Planck-Institute for Astronomy (MPIA), the Max-Planck-Institute for Astrophysics (MPA), New Mexico State University, University of Pittsburgh, University of Portsmouth, Princeton University, the United States Naval Observatory, and the University of Washington.

Facilities: CXO (ACIS), HST (ACS), Max Planck:2.2m (WFI), VLA, ROSAT (PSPC), Sloan

REFERENCES

- Abazajian, K., et al. 2004, *AJ*, 128, 502
 Akritas, M. G., & Siebert, J. 1996, *MNRAS*, 278, 919
 Alexander, D. M., et al. 2003, *AJ*, 126, 539
 Anderson, S. F., & Margon, B. 1987, *ApJ*, 314, 111
 Antonucci, R. 1993, *ARA&A*, 31, 473
 Avni, Y., & Tananbaum, H. 1982, *ApJ*, 262, L17
 Avni, Y., & Tananbaum, H. 1986, *ApJ*, 305, 83
 Barger, A. J., Cowie, L. L., Brandt, W. N., Capak, P., Garmire, G. P., Hornschemeier, A. E., Steffen, A. T., & Wehner, E. H. 2002, *AJ*, 124, 1839
 Barger, A. J., Cowie, L. L., Mushotzky, R. F., Yang, Y., Wang, W.-H., Steffen, A. T., & Capak, P. 2005, *AJ*, 129, 578
 Bauer, F. E., Alexander, D. M., Brandt, W. N., Schneider, D. P., Treister, E., Hornschemeier, A. E., & Garmire, G. P. 2004, *AJ*, 128, 2048
 Bechtold, J., et al. 2003, *ApJ*, 588, 119
 Boyle, B. J., Shanks, T., Croom, S. M., Smith, R. J., Miller, L., Loaring, N., & Heymans, C. 2000, *MNRAS*, 317, 1014
 Brandt, W. N., Laor, A., & Wills, B. J. 2000, *ApJ*, 528, 637
 Buckley, J., & James, I. 1979, *Biometrika*, 66, 429
 Castander, F. J., Treister, E., Maccarone, T. J., Coppi, P. S., Maza, J., Zepf, S. E., & Guzmán, R. 2003, *AJ*, 125, 1689
 Chanan, G. A. 1983, *ApJ*, 275, 45
 Cowie, L. L., Barger, A. J., Bautz, M. W., Brandt, W. N., & Garmire, G. P. 2003, *ApJ*, 584, L57
 Croom, S. M., Smith, R. J., Boyle, B. J., Shanks, T., Miller, L., Outram, P. J., & Loaring, N. S. 2004, *MNRAS*, 349, 1397
 Dempster, A. P., Laird, N. M., & Rubin, D. B. 1977, *Royal Stat. Soc. B*, 39, 1
 De Villiers, J.-P. & Hawley, J. F., 2003, *ApJ*, 589, 458
 Djorgovski, S. G., Gal, R. R., Odewahn, S. C., de Carvalho, R. R., Brunner, R., Longo, G., & Scaramella, R. 1998, in *Wide Field Surveys in Cosmology*, 14th IAP meeting held May 26-30, 1998, Paris. Publisher: Editions Frontieres. ISBN: 2-8 6332-241-9, p. 89., 89
 Feigelson, E. D., & Nelson, P. I. 1985, *ApJ*, 293, 192
 Gialvalisco, M., et al. 2004, *ApJ*, 600, L93
 Green, P. J., et al. 1995, *ApJ*, 450, 51
 Hasinger, G., Miyajiri, T., & Schmidt, M. 2005, *A&A*, 441, 417
 Hawley, J. F., Gammie, C. F., & Balbus, S. A., 1995, *ApJ*, 440, 742
 Henry, J. P., et al. 1994, *AJ*, 107, 1270
 Irwin, M., McMahon, R. G., & Hazard, C. 1991, in *ASP Conf. Ser. 21: The Space Distribution of Quasars*, 117
 Isobe, T., Feigelson, E. D., Akritas, M. G., & Babu, G. J. 1990, *ApJ*, 364, 104
 Isobe, T., Feigelson, E. D., & Nelson, P. I. 1986, *ApJ*, 306, 490
 Jester, S., et al. 2005, *AJ*, 130, 873
 Kellermann, K. I., Fomalont, E. B., Kelly, J., Shaver, P., Rosati, P., Tozzi, P., & Mainieri, V. 2004, *American Astronomical Society Meeting Abstracts*, 205,
 Kelly, B. C., Bechtold, J., Siemiginowska, A., Aldcroft, T., Elvis, M., & Sobolewska, M. 2005, *Memorie della Societa Astronomica Italiana*, 76, 87
 Kembhavi, A., Feigelson, E. D., & Singh, K. P. 1986, *MNRAS*, 220, 51
 Kendall, M. G. 1938, *Biometrika*, 30, 81
 Kendall, M. G. 1970, *Rank Correlation Methods* (Fourth ed.) (Hafner: New York)
 Kriss, G. A., & Canizares, C. R. 1985, *ApJ*, 297, 177
 Krolik, J. H., et al. 2005, *ApJ*, 622, 1008
 La Franca, F., et al. 2005, *ApJ*, 635, 864
 La Franca, F., Franceschini, A., Cristiani, S., & Vio, R. 1995, *A&A*, 299, 19
 Lavalley, M., Isobe, T., & Feigelson, E. 1992, in *ASP Conf. Ser. 25: Astronomical Data Analysis Software and Systems I*, 245
 Lehmer, B. D., et al. 2005, *ApJS*, 161, 21
 Malkan, M. A., Green, R. F., & Hutchings, J. B. 1987, *ApJ*, 322, 729
 Miyajiri, T., Hasinger, G., & Schmidt, M. 2000, *A&A*, 353, 25
 Moran, E. C., Filippenko, A. V., & Chornock, R. 2002, *ApJ*, 579, L71
 Page, K. L., Reeves, J. N., O'Brien, P. T., & Turner, M. J. L. 2005, *MNRAS*, 364, 195
 Pentericci, L., et al. 2003, *A&A*, 410, 75
 Petric, A. O., Carilli, C. L., Bertoldi, F., Fan, X., Cox, P., Strauss, M. A., Omont, A., & Schneider, D. P. 2003, *AJ*, 126, 15
 Richards, G. T., et al. 2005, *MNRAS*, 360, 839
 Richards, G. T., et al. 2003, *AJ*, 126, 1131
 Richards, G. T., et al. 2006, submitted to *AJ*, (astro-ph/0601434)
 Rix, H., et al. 2004, *ApJS*, 152, 163
 Schmidt, M., & Green, R. F. 1983, *ApJ*, 269, 352
 Schneider, D. P., et al. 2005, *AJ*, 130, 367
 Schneider, D. P., Schmidt, M., Hasinger, G., Lehmann, I., Gunn, J. E., Giacconi, R., Trümper, J., & Zamorani, G. 1998, *AJ*, 115, 1230
 Shemmer, O., Brandt, W. N., Vignali, C., Schneider, D. P., Fan, X., Richards, G. T., & Strauss, M. A. 2005, *ApJ*, 630, 729
 Silverman, J. D., et al. 2005a, *ApJ*, 624, 630
 Silverman, J. D., et al. 2005b, *ApJ*, 618, 123
 Silverman, J. D., et al. 2002, *ApJ*, 569, L1
 Steffen, A. T., Barger, A. J., Capak, P., Cowie, L. L., Mushotzky, R. F., & Yang, Y. 2004, *AJ*, 128, 1483
 Steffen, A. T., Barger, A. J., Cowie, L. L., Mushotzky, R. F., & Yang, Y. 2003, *ApJ*, 596, L23
 Strateva, I. V., Brandt, W. N., Schneider, D. P., Vanden Berk, D. G., & Vignali, C. 2005, *AJ*, 130, 387
 Tananbaum, H., et al. 1979, *ApJ*, 234, L9
 Treister, E., Castander, F. J., Maccarone, T. J., Herrera, D., Gawiser, E., Maza, J., & Coppi, P. S. 2004, *ApJ*, 603, 36
 Ueda, Y., Akiyama, M., Ohta, K., & Miyajiri, T. 2003, *ApJ*, 598, 886
 Uttley, P., & McHardy, I. M. 2004, *Progress of Theoretical Physics Supplement*, 155, 170
 Vanden Berk, D. E., et al. 2001, *AJ*, 122, 549

- Véron-Cetty, M.-P., & Véron, P. 2003, *A&A*, 412, 399
 Vignali, C., Brandt, W. N., Fan, X., Gunn, J. E., Kaspi, S., Schneider, D. P., & Strauss, M. A. 2001, *AJ*, 122, 2143
 Vignali, C., Bauer, F. E., Alexander, D. M., Brandt, W. N., Hornschemeier, A. E., Schneider, D. P., & Garmire, G. P. 2002, *ApJ*, 580, 105
 Vignali, C., Brandt, W. N., & Schneider, D. P. 2003, *AJ*, 125, 433
 Vignali, C., Brandt, W. N., Schneider, D. P., & Kaspi, S. 2005, *AJ*, 129, 2519
 Walter, R., & Fink, H. H. 1993, *A&A*, 274, 105
 Wilkes, B. J., & Elvis, M. 1987, *ApJ*, 323, 243
 Wilkes, B. J., Tananbaum, H., Worrall, D. M., Avni, Y., Oey, M. S., & Flanagan, J. 1994, *ApJS*, 92, 53
 Wolf, C., et al. 2004, *A&A*, 421, 913
 Wolf, C., Wisotzki, L., Borch, A., Dye, S., Kleinheinrich, M., & Meisenheimer, K. 2003, *A&A*, 408, 499
 Worrall, D. M., & Birkinshaw, M. 2005, in *Physics of Active Galactic Nuclei at All Scales*, ed. A. D., J. R., & L. P. (Springer-Verlag, Berlin), in press; astro-ph/0410297
 Worrall, D. M., Tananbaum, H., Giommi, P., & Zamorani, G. 1987, *ApJ*, 313, 596
 Yang, Y., Mushotzky, R. F., Steffen, A. T., Barger, A. J. & Cowie, L. L. 2004, *AJ*, 128, 1501
 York, D. G., et al. 2000, *AJ*, 120, 1579
 Yuan, W., Siebert, J., & Brinkmann, W. 1998, *A&A*, 334, 498
 Zheng, W., et al. 2001, *ApJ*, 562, 152
 Zickgraf, F.-J., et al. 1997, *A&A*, 323, L21

APPENDIX

A. PROPERTIES OF ADDITIONAL $z > 4$ AGNS

We list the properties of the publicly available sources from Kelly et al. (2005) in Table A1. To our knowledge, details on these sources are not available in the literature. The *Chandra* data were reduced using the same methods outlined in Vignali et al. (2001). In Table A2, we list the properties of the X-ray–selected AGN presented in § 2.2.3.

TABLE A1
 PROPERTIES OF $z > 4$ QUASARS OBSERVED BY *Chandra*

Object (1)	z (2)	N_{H} (3)	AB_{1450} (4)	f_{2500} (5)	$\log(L_{2500})$ (6)	M_B (7)	Exp. Time (8)	Count rate (9)	f_{SB} (10)	$f_{2\text{keV}}$ (11)	$\log(\nu L_{\nu})_{2\text{keV}}$ (12)	$\log(L_{\text{HB}})$ (13)	α_{ox} (14)	R (15)
QSO 0910+564	4.04	2.73	20.7	3.08	30.98	-25.9	22849	$0.34^{+0.17}_{-0.32}$	$1.32^{+0.67}_{-0.45}$	0.99	44.18	44.4	-1.72 ± 0.09	< 16.6
PC 1450+3404	4.19	1.26	21.0	2.33	30.89	-25.7	14842	$0.94^{+0.32}_{-0.25}$	$3.49^{+1.21}_{-0.93}$	2.71	44.64	44.9	$-1.51^{+0.08}_{-0.07}$	< 20.3
SDSS 1413+0000	4.08	3.12	19.8	7.05	31.35	-26.8	11843	$1.17^{+0.40}_{-0.32}$	$4.61^{+1.58}_{-1.25}$	3.49	44.74	44.9	-1.65 ± 0.07	< 7.4
SDSS 0050-0053	4.33	2.69	19.5	9.73	31.53	-27.3	12737	$1.15^{+0.39}_{-0.29}$	$4.24^{+1.44}_{-1.08}$	3.38	44.75	44.9	-1.71 ± 0.07	< 5.6
SDSS 1444-0123	4.18	3.92	19.5	9.64	31.50	-27.2	10001	$0.40^{+0.32}_{-0.19}$	$1.60^{+1.28}_{-0.76}$	1.24	44.30	44.5	$-1.87^{+0.11}_{-0.12}$	< 5.4
SDSS 2357+0043	4.36	3.28	19.8	7.38	31.41	-27.0	12657	$0.85^{+0.35}_{-0.25}$	$3.47^{+1.43}_{-1.03}$	2.73	44.67	44.9	-1.70 ± 0.08	< 7.0

NOTE. — (1) Source name; (2) Redshift; (3) Galactic column density, from Dickey & Lockman (1990), in units of 10^{20} cm^{-2} ; (4) AB magnitude at rest-frame 1450 Å; (5) flux density at rest-frame 2500 Å, in units of $10^{-28} \text{ erg cm}^{-2} \text{ s}^{-1} \text{ Hz}^{-1}$; (6) log of the monochromatic luminosity at rest-frame 2500 Å, in units of $\text{erg s}^{-1} \text{ Hz}^{-1}$; (7) absolute B -band magnitude; (8) *Chandra* exposure times (in seconds) corrected for detector dead time and high-background periods; (9) observed count rate computed in the soft band, in units of $10^{-3} \text{ counts s}^{-1}$; (10) Galactic absorption-corrected flux in the observed 0.5–2 keV band, in units of $10^{-15} \text{ erg cm}^{-2} \text{ s}^{-1}$; (11) rest-frame 2 keV flux density, in units of $10^{-32} \text{ erg cm}^{-2} \text{ s}^{-1} \text{ Hz}^{-1}$; (12) log of the luminosity at rest-frame 2 keV, in units of erg s^{-1} ; (13) log of the 2–10 keV rest-frame luminosity, corrected for the effect of Galactic absorption, in units of erg s^{-1} ; (14) optical-to-X-ray spectral index; errors have been computed following the “numerical method” described in § 1.7.3 of Lyons (1991); both the statistical uncertainties on the X-ray count rates and the effects of the observed ranges of the X-ray and optical continuum shapes have been taken into account; (15) radio loudness parameter, defined as $R = f_5 \text{ GHz} / f_{4400 \text{ Å}}$ (rest frame). The 5 GHz flux density is computed from the 1.4 GHz flux density (from FIRST) assuming a radio power-law slope of $\alpha = -0.8$, with $f_{\nu} \propto \nu^{\alpha}$.

TABLE A2
 PROPERTIES OF X-RAY–SELECTED, $z > 4$ AGNS

Object (1)	z (2)	N_{H} (3)	AB_{1450} (4)	f_{2500} (5)	$\log(L_{2500})$ (6)	f_{SB} (7)	$f_{2\text{keV}}$ (8)	$\log(L_{2\text{keV}})$ (9)	α_{ox} (10)	Reference (11)
CXOCY J033716.7-050153	4.61	4.82	23.8	-28.84	29.74	1.8	-31.82	26.76	-1.14	Treister et al. (2004)
CLASXS J1032414.2+572227	5.40	0.73	24.3	-29.04	29.65	0.85	-32.09	26.60	-1.17	Steffen et al. (2004); Yang et al. (2004)
RX J1052+5719	4.45	0.56	22.6	-28.36	30.20	2.3	-31.73	26.83	-1.29	Schneider et al. (1998)
CXOMP J105655.1-034322	4.05	3.55	22.3	-28.24	30.26	5.2	-31.37	27.13	-1.20	Silverman et al. (2005b)
CXOHDFN J123647.9+620941	5.19	1.48	23.5	-28.72	29.94	0.29	-32.57	26.09	-1.48	Barger et al. (2002); Vignali et al. (2002)
CXOHDFN J123719.0+621025	4.14	1.45	25.2	-29.40	29.11	0.26	-32.70	25.81	-1.26	Barger et al. (2002); Vignali et al. (2002)
CXOCY J125304.0-090737	4.18	2.96	23.0	-28.52	30.00	1.7	-31.88	26.64	-1.28	Castander et al. (2003)
CXOMP J213945.0-234655	4.93	3.55	21.6	-27.96	30.67	1.8	-31.80	26.83	-1.47	Silverman et al. (2002)

NOTE. — (1) Source name (in order of increasing Right Ascension); (2) Redshift; (3) Galactic column density, from Dickey & Lockman (1990), in units of 10^{20} cm^{-2} ; (4) AB magnitude at rest-frame 1450 Å; (5) log of the flux density at rest-frame 2500 Å, in units of $\text{erg cm}^{-2} \text{ s}^{-1} \text{ Hz}^{-1}$; (6) log of the monochromatic luminosity at rest-frame 2500 Å, in units of $\text{erg s}^{-1} \text{ Hz}^{-1}$; (7) Galactic absorption-corrected flux in the observed 0.5–2 keV band, in units of $10^{-15} \text{ erg cm}^{-2} \text{ s}^{-1}$; (8) log of the rest-frame 2 keV flux density, in units of $\text{erg cm}^{-2} \text{ s}^{-1} \text{ Hz}^{-1}$; (9) log of the monochromatic luminosity at rest-frame 2 keV, in units of $\text{erg s}^{-1} \text{ Hz}^{-1}$; (10) optical-to-X-ray spectral index; (11) References for X-ray–selected AGN.